A SYSTEMATIC ANALYSIS OF Fe II EMISSION IN QUASARS: EVIDENCE FOR INFLOW TO THE CENTRAL BLACK HOLE

Chen Hu[1,2,3], Jian-Min Wang[2], Luis C. Ho[4], Yan-Mei Chen[2,3], Hao-Tong Zhang[1], Wei-Hao Bian[2,5] and Sui-Jian Xue[1]
Accepted for publication in ApJ.

ABSTRACT

Broad Fe II emission is a prominent feature of the optical and ultraviolet spectra of quasars. We report on a systematical investigation of optical Fe II emission in a large sample of 4037 $z < 0.8$ quasars selected from the Sloan Digital Sky Survey. We have developed and tested a detailed line-fitting technique, taking into account the complex continuum and narrow and broad emission-line spectrum. Our primary goal is to quantify the velocity broadening and velocity shift of the Fe II spectrum in order to constrain the location of the Fe II-emitting region and its relation to the broad-line region. We find that the majority of quasars show Fe II emission that is redshifted, typically by ~ 400 km s^{-1} but up to 2000 km s^{-1}, with respect to the systemic velocity of the narrow-line region or of the conventional broad-line region as traced by the Hβ line. Moreover, the line width of Fe II is significantly narrower than that of the broad component of Hβ. We show that the magnitude of the Fe II redshift correlates inversely with the Eddington ratio, and that there is a tendency for sources with redshifted Fe II emission to show red asymmetry in the Hβ line. These characteristics strongly suggest that Fe II originates from a location different from, and most likely exterior to, the region that produces most of Hβ. The Fe II-emitting zone traces a portion of the broad-line region of intermediate velocities whose dynamics may be dominated by infall.

Subject headings: galaxies: nuclei — (galaxies:) quasars: emission lines — (galaxies:) quasars: general — galaxies: Seyfert — line: profiles

1. INTRODUCTION

Fe emission contributes significantly to the optical and ultraviolet (UV) spectra of most active galactic nuclei (AGNs), both in terms of wavelength coverage and flux. The properties of the Fe II-emitting clouds may provide important clues to the underlying physics in the broad-line region (BLR). First, Fe II emission can be used to constrain the covering factor of BLR clouds from energy budget considerations. Second, the ratio of the equivalent width (EW) of Fe II to that of H$\beta_{\rm BC}$ strongly varies with statistical measures of AGN correlations, such as the so-called Eigenvector 1 derived from principal component analysis, which is believed to be driven by some fundamental property such as mass accretion rate (e.g., Boroson & Green 1992; Sulentic et al. 2000a,b; Marziani et al. 2001, 2003a). Third, Fe abundance derived from Fe II emission can be used to study the cosmological evolution of AGNs and possibly chemical enrichment of their hosts and environment (e.g., Wills et al. 1985; Wheeler et al. 1989; Dietrich et al. 2002, 2003; Maiolino et al. 2003). Careful measurement of the properties of Fe II emission in a large sample of AGNs will clearly have a considerable impact on our understanding of these systems.

The origin of the optical/UV Fe emission has been hotly debated for more than two decades. Thousands of Fe emission lines blend together to form a pseudo-continuum, which, when combined with Balmer continuum emission, results in the "small blue bump" around 3000 Å (Grandi 1982; Wills et al. 1985). Previously, theoretical calculations of photoionized clouds in the BLR encountered difficulties reproducing the observed strength of strong Fe II emission, prompting many authors to propose additional physical mechanisms (Netzer & Wills 1983; Wills et al. 1985; Joly 1987, 1991; Collin-Souffrin et al. 1988; Sigut & Pradhan 1998). Recently, a more sophisticated calculation by Baldwin et al. (2004) revealed that the predicted shape and EW of the 2200–2800Å Fe II UV bump can only be made consistent with observed values if either microturbulence of hundreds of km s^{-1} or another collisionally excited component is included in the model.

Despite its significance, current observations of Fe II emission provide poor constraints on its origin. Some studies suggest that Fe II emission originates from the same region as the other broad emission lines. For example, Phillips (1977), Boroson & Green (1992), Laor et al. (1997b), and Véron-Cetty et al. (2004) observed similar line widths and profiles for Fe II and H$\beta_{\rm BC}$, and Maoz et al. (1993) found that both Fe II emission and the Balmer continuum have comparable variation amplitudes. But there is a growing debate on this issue. Marziani et al. (2003b) found that H$\beta_{\rm BC}$ is systematically broader than Fe II for sources with FWHM(H$\beta_{\rm BC}$) > 4000 km s^{-1}. Recent studies of Fe II emission variability have shown that Fe II emission responds to variations in continuum flux but that the variability amplitude of Fe II is not the same as that of Hβ (Vestergaard & Peterson 2005 and references therein; Wang et al. 2005; Kuehn et al. 2008). In fact, the upper limit on the time lag between Fe II emission and the continuum exceeds the lag of any other observed emission lines obtained (Vestergaard & Peterson 2005). This implies that Fe II may be emitted from further out in the BLR than any other broad emission line. Kuehn et al. (2008) suggested that Fe II may be produced from a region between the BLR and the dust sublimation radius. The study of Matsuoka et al. (2008), based on measurements of the O I and Ca II emis-

[1] National Astronomical Observatories of China, Chinese Academy of Sciences, Beijing 100012, China; chenhu@bao.ac.cn
[2] Key Laboratory for Particle Astrophysics, Institute of High Energy Physics, Chinese Academy of Sciences, Beijing 100039, China.
[3] Graduate University of the Chinese Academy of Sciences, Beijing 100049, China.
[4] The Observatories of the Carnegie Institution of Washington, 813 Santa Barbara Street, Pasadena, CA 91101, USA.
[5] Department of Physics and Institute of Theoretical Physics, Nanjing Normal University, Nanjing 210097, China.

sion lines, supports the notion that Fe II emerges from the outer portion of the BLR. In a recent three-dimensional spectroscopic study of Mrk 493, Popović et al. (2007) found that the Fe II emission region is extensive and that the line width of Fe II is only 1/3 of that of H$\beta_{\rm BC}$, leading them to suggest that Fe II emission originates in an intermediate-line region. If these findings can be confirmed, Fe II emission can be a probe of the intermediate-line region, which may be the transition from the torus to the BLR and accretion disk.

Quasar emission lines often exhibit considerable velocity shifts with respect to each other. However, the relative velocity of Fe II emission with respect to other lines has not been well studied, especially in systematically for a large sample of objects (only a few measurements of individual sources have been published; e.g., Véron-Cetty et al. 2004). In fact, almost all broad quasar emission lines show blueward velocity shifts (Gaskell 1982; Carswell et al. 1991), with the exception of Mg II (no shift; Junkkarinen 1989) and Hβ (redward shift in some studies; e.g., McIntosh et al. 1999). Most previous studies simply *assumed* that Fe II has no shift with respective to [O III] (e.g., Boroson & Green 1992; Marziani et al. 1996; McLure & Jarvis 2002; Dietrich et al. 2003; Greene & Ho 2005b; Kim et al. 2006; Woo et al. 2006) and that it has the same line width as the broad component of Hβ (e.g., Netzer & Trakhtenbrot 2007; Salviander et al. 2007). The goal of this study is to test this assumption.

The present paper presents the first detailed investigation of the velocity shift and width of optical Fe II emission[6] in a large sample of quasars selected from the Sloan Digital Sky Survey (SDSS; York et al. 2000). Our primary motivation is to determine the physical location and origin of the Fe II-emitting region. We describe selection of the sample in §2 and spectral analysis in §3. We test the reliability of the measurements and the errors using Monte Carlo simulations (§3.3), and then check how significantly our method improves the spectral fit and how our method affects the measurements of other emission-line parameters (§3.4). Section 4 discusses the results we obtained, including the distribution of Fe II emission shifts and widths, correlations with other parameters, and also an analysis of the composite spectra. The implications of our results are discussed in §5, with concluding remarks given in §6.

Throughout this work, we adopt the following cosmological parameters: $H_0 = 70$ km s^{-1} Mpc^{-1}, $\Omega_m = 0.3$, and $\Omega_\Lambda = 0.7$ (Spergel et al. 2007).

2. SAMPLE SELECTION

Our sample is selected from the SDSS Fifth Data Release (DR5; Adelman-McCarthy et al. 2007) quasar catalog (Schneider et al. 2007). We choose objects with redshift $z < 0.8$ to ensure that the [O III] emission line lies within the SDSS spectral coverage. Since the SDSS quasar sample is flux-limited and selected by broad-band colors (Richards et al. 2002a), care must be exercised in using it to study the quasar luminosity function (Vanden Berk et al. 2005; Richards et al. 2006) or its cosmological evolution. However, this sample is adequate for the scientific goals of this work.

We impose a series of selection criteria to ensure reliable measurements of Fe II emission. (1) We require a signal-to-noise ratio (S/N) >10 in the wavelength range 4430–5550

Å, covering Hβ, [O III], and the most prominent features of optical Fe II emission. (2) We remove sources that have reduced $\chi^2 > 4$ in the continuum decomposition (§3.1.3). These sources cannot be fitted well by the present continuum model (Eq. (1) in §3.1). (3) We remove sources that have EW$_{\rm Fe} < 25$ Å; this EW cut is determined by the simulations described in §3.3. (4) We also remove sources with H$\beta_{\rm BC}$ FWHM errors >10% and [O III] λ5007 peak velocity shift errors >100 km s^{-1}. In total, the final sample contains 4037 sources, which is roughly 30% of all quasars in DR5 with redshift $z < 0.8$.

3. SPECTRAL FITTING

The spectra of quasars from UV to optical wavelengths are remarkably similar to each other. The quasar composite spectrum (e.g., Vanden Berk et al. 2001) is characterized by a featureless continuum and a plethora of broad and narrow emission lines. In the luminosity range of interest to us here, very little, if any, starlight is observed, so we can ignore the host galaxy contribution to the spectrum. The validity of this simplification can be tested from our spectral fitting—nearly all of the sources in the sample can be well fitted without a host galaxy component.

The procedure of our spectral fitting algorithm is as follows. We begin by deredshifting the spectrum after correcting for Galactic extinction. Then, the continuum is decomposed into three components: (1) a single power law, (2) Balmer continuum emission (supplemented with high-order Balmer emission lines), and (3) a pseudo-continuum due to blended Fe emission. We subtract this continuum model to obtain a pure emission-line spectrum, which is then fitted to derive parameters for the emission lines. The measurement of Fe emission is strongly affected by the uncertainty in the determination of the continuum level. Since there are almost no "pure" continuum windows, a simultaneous fit should be performed to decouple the Fe emission from the featureless continuum, rather than fitting the two independently. [Tsuzuki et al. (2006) adopt an alternative approach in which they use a theoretical model to estimate the flux fraction of the emission lines in the continuum windows.] The following subsections will describe each step in detail.

3.1. *Continuum Decomposition*

We use the R_V-dependent Galactic extinction law given by Cardelli et al. (1989) and assume $R_V = 3.1$. Eqs. (2a) and (2b) in Cardelli et al. (1989) are used for the infrared band, but Eqs. (3a) and (3b) are replaced by those in O'Donnell (1994) for the optical band. We adopt the Galactic extinction in the u band listed in the SDSS quasar catalog (Schneider et al. 2007) and change it to the V band using the relation $A_V = A_u/1.579$ (Schlegel et al. 1998). Then, we deredshift the extinction-corrected spectrum using the redshift provided by the SDSS pipeline. This value of redshift is later refined using the line centroid of [O III] λ5007 measured after continuum decomposition (see §3.5).

We model the continuum of the spectrum after Galactic extinction and redshift correction (hereinafter the corrected spectrum) using three components:

$$F_\lambda = F_\lambda^{\rm PL}(F_{5100}, \alpha) + F_\lambda^{\rm BaC}(F_{\rm BE}, \tau_{\rm BE})$$
$$+ F_\lambda^{\rm Fe}(F_{\rm Fe}, {\rm FWHM}_{\rm Fe}, V_{\rm Fe}). \qquad (1)$$

In total there are seven free parameters. The first term is the featureless power law

$$F_\lambda^{\rm PL} = F_{5100} \left(\frac{\lambda}{5100} \right)^\alpha, \qquad (2)$$

---

where F_{5100} is the flux density at 5100 Å and α is the spectral index. The second and third terms denote the Balmer continuum and Fe emission, respectively, which are described below. For the Fe emission term, F_{Fe} is the flux and V_{Fe} is the shift velocity of Fe II.

3.1.1. *Balmer Continuum and High-order Balmer Lines*

Following Grandi (1982) and Dietrich et al. (2002), the Balmer continuum produced by a partially optically thick cloud with a uniform temperature can be expressed by

$$F_\lambda^{BaC} = F_{BE} B_\lambda(T_e)(1 - e^{-\tau_\lambda}) \qquad (3)$$

for wavelengths shortward of the Balmer edge ($\lambda_{BE} = 3646$ Å). $B_\lambda(T_e)$ is the Planck function at an electron temperature T_e, F_{BE} is a normalization coefficient for the flux at λ_{BE}, and τ_λ is the optical depth at λ expressed by

$$\tau_\lambda = \tau_{BE}\left(\frac{\lambda}{\lambda_{BE}}\right), \qquad (4)$$

where τ_{BE} is the optical depth at the Balmer edge. There are two free parameters, F_{BE} and τ_{BE}. Following Dietrich et al. (2002), we assume $T_e = 15,000$ K.

At wavelengths $\lambda > \lambda_{BE}$, blended higher-order Balmer lines give a smooth rise in the spectrum from ~ 4000 Å to the Balmer edge (Wills et al. 1985). We treat the higher-order Balmer lines in a manner similar to that in Dietrich et al. (2003), with some modifications. To determine the relative strengths of the transitions with $7 \leq n \leq 50$, we use the line emissivities given by Storey & Hummer (1995) for Case B, $T_e = 15,000$ K, and $n_e = 10^8$ cm^{-3}. We normalize the flux of the higher-order Balmer lines to the flux of the Balmer continuum at the edge using the results in Wills et al. (1985). (This implies that the higher-order Balmer lines also depend on F_{BE} and τ_{BE}.) In order to smooth the rise to the Balmer edge, we assume that each line has a Gaussian profile with FWHM = 8000 km s^{-1}. In practice, none of the assumptions concerning the higher-order Balmer lines actually impact our results because our fitting windows do not include this region (see §3.1.3).

3.1.2. *Fe Emission*

Phillips (1977) first introduced the template-fitting method to treat Fe emission in AGNs, using the Fe spectrum of the narrow-line Seyfert 1 (NLS1) galaxy I Zw 1 ($z = 0.061$) to construct an Fe II template. In most applications of this method, the amount of velocity broadening applied to the template during spectral fitting is either solved as a free parameter or is fixed (usually to the FWHM of broad Hβ). But the Fe template itself is not allowed to shift in velocity. We follow essentially the same template-fitting, but we explicitly allow the width and shift of Fe II to be free parameters. We now describe the details of our algorithm.

Considering the redshift range of our sample, we need both the UV and optical Fe template for I Zw 1. In the UV band, we adopt the Fe template of Vestergaard & Wilkes (2001). Note that their template is set to zero around the Mg II line, which is unphysical. However, the Mg II line is not the main focus of the present work, and for the purposes of this work we do not concern ourselves with this complication. In the optical, apart from the widely used template constructed by Boroson & Green (1992), some others are also available. For example, a template of any width can be constructed from the list of Fe lines for I Zw 1 given by Véron-Cetty et al. (2004).

We compared these two different templates and in the end chose the one from Boroson & Green (1992) (kindly provided by T. A. Boroson) because it gives smaller reduced χ^2. However, we have verified that the shift of Fe emission, one of the main goals of this work, is actually not sensitive to the choice of template. The velocity shifts measured using either of the two template are consistent with each other.

We combine the UV and optical templates to form a single template (with a gap from 3100 Å to 3700 Å, which has no data) and convolve it with a Gaussian function:

$$F_\lambda^{Fe} = F_\lambda^{IZw1} * G(F_{conv}, FWHM_{conv}, V_{conv}), \qquad (5)$$

where F_λ^{IZw1} is the I Zw 1 Fe template, G is a Gaussian function with flux F_{conv}, width $FWHM_{conv}$, and peak velocity shift V_{conv}. The convolution is done in logarithmic wavelength space because $d(\ln\lambda) = d\lambda/\lambda = dv/c$. The parameters in Eq. (1) can be calculated as follows. The flux of the Fe emission, F_{Fe}, is equal to F_{conv} multiplied by the flux of the template. The shift of the Fe spectrum, V_{Fe}, is simply V_{conv}. Finally, the FWHM of the Fe lines can be expressed as

$$FWHM_{Fe} = \sqrt{FWHM_{IZw1}^2 + FWHM_{conv}^2} \quad . \qquad (6)$$

In the above algorithm, we assume that the Fe emission in the UV and optical have the same width and velocity shift, and that the ratio of UV Fe flux to optical Fe flux is fixed to that of I Zw 1. These assumptions help to reduce the number of free parameters, and seem appropriate given the S/N of the present sample. If we split the UV/optical template following Verner et al. (2004) to three major wavelength bands—UV (2000–3000 Å), small blue bump (3000–3500 Å), and optical (4000–6000 Å)—the final results will be determined mainly by the optical Fe emission. The reasons are as follows. First, the small blue bump Fe emission is outside of our fitting windows (see §3.1.3). Second, the spectra of most of the quasars in the sample either do not cover or only cover a very narrow segment of the UV Fe emission wavelength range. Third, the S/N of the UV band is lower than the optical band. Thus, our measurements mainly trace the optical Fe emission and are not very sensitive to UV Fe emission. We consider each of the three assumptions in turn.

The ratio of UV to optical Fe flux has been investigated by many authors (e.g., Sigut et al. 2004; Verner et al. 2004; Baldwin et al. 2004, and references therein). This ratio depends on the physical parameters of the clouds, such as the hydrogen density n_H, the hydrogen-ionizing flux Φ_H, the velocity of turbulence, and so forth. However, for physical conditions typical of quasars ($n_H \approx 10^{11}$ cm^{-3}, $\Phi_H \approx 3 \times 10^{20}$ cm^{-2} s^{-1}; Ferland et al. 1992), models of Fe emission indicate that there are large regions of parameter space where the ratio is roughly constant (Figs. 3 and 4. in Verner et al. 2004). This suggests that adopting a single ratio of UV to optical Fe flux (fixed to that of I Zw 1) should be a reasonably good approximation.

The width of the UV Fe lines is also not necessarily equal to that of the optical Fe lines. Many authors fix the width of the optical Fe lines to the width of broad Hβ_{BC}, while in the UV the width is fixed to that of Mg II (e.g., Salviander et al. 2007). This procedure implicitly assumes that the optical Fe lines and Hβ_{BC} originate from the same region, and similarly that the UV Fe lines follow Mg II. Empirically, however, the width of Hβ_{BC} is consistent with that of Mg II (McLure & Jarvis 2002); the difference is only 0.05 dex on average (Salviander et al. 2007). Our results in §4.2 also show

this. Thus, for the present purposes, it is safe to assume one single value for the width of the optical and UV Fe lines. We leave the width as a free parameter, as has been done in many previous studies (e.g., McLure & Jarvis 2002; Dietrich et al. 2003; Kim et al. 2006).

The velocity shift of the UV Fe lines[7] could be different from that of the optical lines if they arise from different regions. We use only the optical Fe template and fit the continuum only in the optical band for testing. The resulting Fe shifts change little, demonstrating that our measurements are mainly determined by the optical Fe lines. Thus, for our goal of studying the optical Fe lines, assuming one single shift for the UV and optical Fe lines is an adequate approximation.

It should be noted here that because of the two reasons mentioned above (low S/N around UV Fe lines and incomplete wavelength near), the present paper cannot conclude whether the UV and optical Fe II have a common origin.

3.1.3. *Multicomponent Fit*

The continuum model described by Eq. (1) is fitted by minimizing the quantity

$$\chi^2 = \sum_i \left(\frac{y_i - y_{\mathrm{model}}}{\sigma_i} \right)^2, \qquad (7)$$

where σ_i is the error of the data set (x_i, y_i). We adopt the Levenberg-Marquardt method (Press et al. 1992, chap. 15.5) to solve Eq. (1), which is nonlinear. We also use it in fitting the emission lines (§3.2). The fitting is performed in the following windows: 2470–2625, 2675–2755, 2855–3010, 3625–3645, 4170–4260, 4430–4770, 5080–5550, 6050–6200, and 6890–7010 Å. These windows are devoid of strong emission lines (Vestergaard & Wilkes 2001; Kim et al. 2006). The window 3625-3645 Å is used to constrain the Balmer continuum emission, because in this region there is no strong Fe emission (Wills et al. 1985). The reduced χ^2 distribution has a median value of $\chi^2 = 1.365$.

Two examples of continuum decomposition are shown in Figures 1 and 2. The top panel shows the corrected spectrum. The spectrum in the fitting window is plotted in green. Each component is plotted in blue and the summed continuum in red. The middle panel shows the residual spectrum, which is the pure emission-line spectrum for the next step (§3.2). The model fits the spectrum very well except in the region $\sim$ 3100–3700 Å, where no Fe template is available. In fact, the total flux of the residual spectrum in this region strongly correlates with the Fe flux F_{Fe}. This is consistent with the "small blue bump" being produced by Fe lines and the Balmer continuum (Wills et al. 1985). We subtract the power law and the Balmer continuum from the corrected spectrum and show the enlarged resultant spectrum (Fe-only spectrum) in the wavelength range 4100–5600 Å in the bottom panel. The Fe model is plotted in red.

From the first example on SDSS J115507.61+520129.6, which has narrow Fe lines, the Fe model not only agrees with the Fe-only spectrum in our fitting windows (in green), but it also fits the two strong Fe II lines at 4924 and 5018 Å very well, even though these two lines are not in the fitting windows. Two blue dashed lines in the middle panel mark the

positions of Hβ λ4861 and [O III] λ5007. The blue dashed line in the bottom panel marks the position of Fe II λ4924 line with zero velocity shift. The shift of Fe emission in this source can be seen clearly from the position of the Fe II λ4924 line; the velocity shift, as measured from the model and with respect to [O III], is 459±16 km s^{-1}. For the second source, SDSS J112611.63+425246.4, Fe II λ4924 cannot be distinguished from [O III] λ4959 but the shift can be seen from the Fe II model. In this case, it is 1691±119 km s^{-1}.

3.2. *Emission-line Fitting*

After subtracting the continuum, we measure the Hβ and [O III] emission lines from the pure emission-line spectrum. We use multiple components to fit the emission lines over the wavelength range 4770–5080 Å. The narrow Hβ component, [O III] λ4959, and [O III] λ5007 are modeled using three Gaussian. The [O III] $\lambda\lambda$4959, 5007 lines are forced to have the same FWHM and no relative wavelength shift, and their intensity ratio fixed to the theoretical value of 3.0. The narrow Hβ component (Hβ_{NC}) is forced to have the same FWHM as [O III] λ5007, a shift of up to 600 km s^{-1} relative to [O III] λ5007, and an intensity constrained to lie between 1/20 and 1/3 of that of [O III] λ5007 (e.g. Veilleux & Osterbrock 1987; McGill et al. 2008). If necessary, we add another two Gaussian components for [O III] $\lambda\lambda$4959, 5007 to match their wings, and a corresponding Gaussian is added to Hβ_{NC} to ensure that Hβ_{NC} and [O III] have the same profile. Following Salviander et al. (2007) and McGill et al. (2008), the broad Hβ component is modeled using a Gauss-Hermite function (van der Marel & Franx 1993), whose best fit yields the FWHM, peak velocity shift, and the square root of the second moment ($\sigma_{\mathrm{H}\beta}$). As illustration, Figure 3 shows the emission-line fitting for the two sources in Figures 1 and 2. The top panel shows the pure emission-line spectrum. The multiple components are in blue and the sum of them is in red; the bottom panel is the residuals.

We also measure the [O II] and Mg II emission lines when they are available. Since the continuum around [O II] is not well determined (we make two assumptions in the model for the higher-order Balmer lines; see the last paragraph in §3.1.1), we simply fit [O II] above a locally defined continuum with a single Gaussian (Greene & Ho 2005a). As many sources have weak [O II] emission, we adopt as detection criterion that the line must have an amplitude larger than 3 times the standard deviation of the local continuum. The Mg II $\lambda\lambda$2796, 2803 doublet is fitted using two Gauss-Hermite functions; they have the same parameters except that the intensity ratio between them is fixed to 2 (Baldwin et al. 1996). The FWHMs and velocity shifts of Mg II are calculated from a single Gauss-Hermite function.

3.3. *Tests of the Continuum Decomposition*

The template-fitting method for measuring Fe emission and the Levenberg-Marquardt algorithm for nonlinear fitting are widely used as almost "standard" approaches. We add a new parameter V_{Fe} and set FWHM$_{\mathrm{Fe}}$ free in our fitting. Since the S/N of the majority of the sources in our sample are low (about 50% have S/N < 15), it is necessary to test the reliability of the Fe emission measurement. We perform a suite of simulations similar to those done in Greene & Ho (2006). Using a Monte Carlo method to generate artificial spectra, we measure the Fe emission of these spectra using the same method as that used for the observed spectra. Differences be-

---

[7] In fact, the velocity shift of each individual UV Fe line may be different. Vestergaard & Wilkes (2001) measured the velocity of each UV Fe line and showed that their shifts can vary by as much as $\sim$ 100 km s^{-1}. But considering the resolution of our spectra, assuming a single velocity shift is safe, both for the UV and optical.
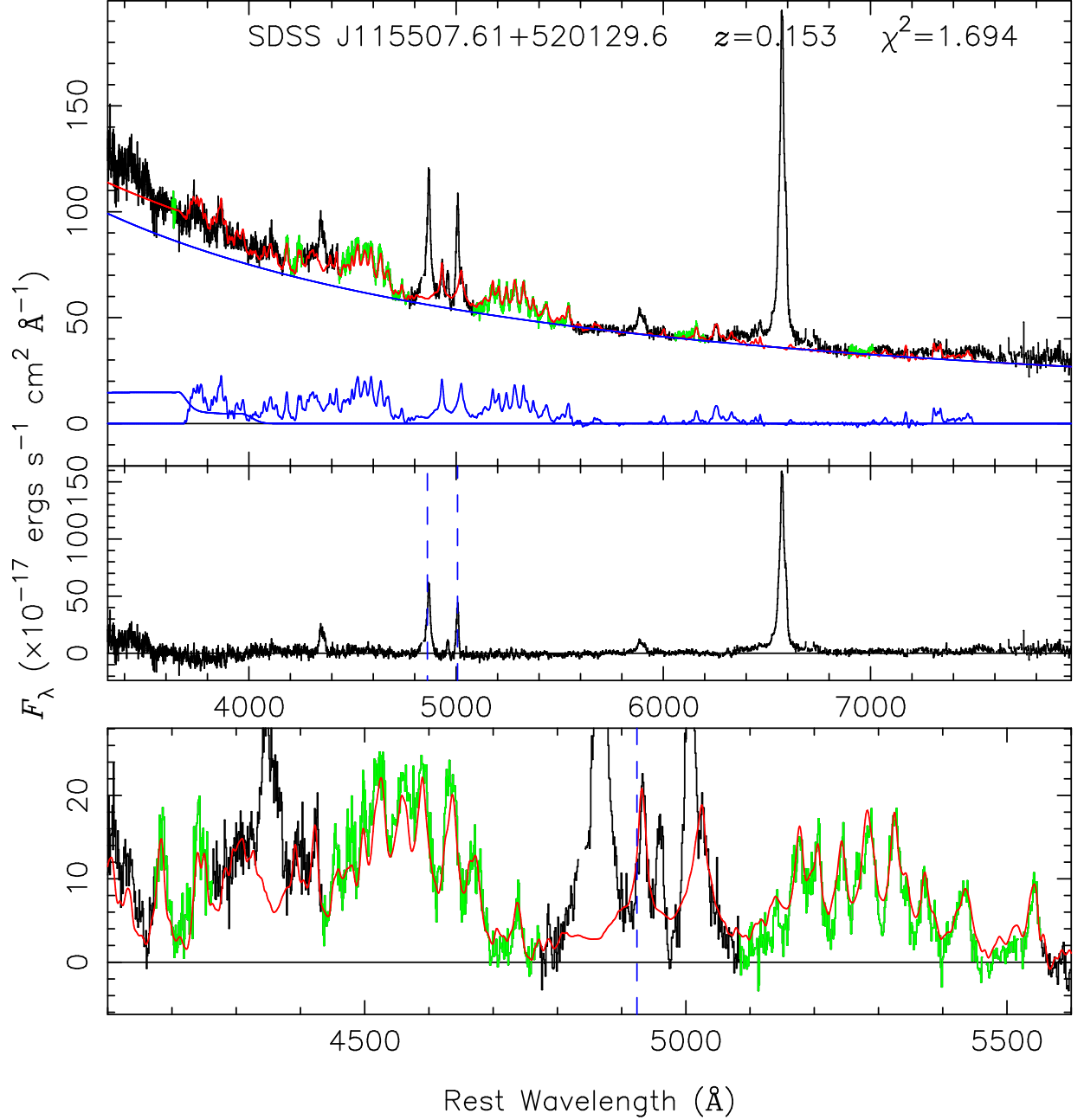
Fig. 1.— Example of continuum decomposition for SDSS J115507.61+520129.6, which has narrow Fe lines. Its v_{Fe} is 459±16 km s^{-1}. Note that our Fe model fits the two strong Fe II lines at 4924 and 5018 Å very well, even though these two lines are not in the fitting window. The top panel gives the spectrum after Galactic extinction and redshift correction. The spectrum in the fitting window is plotted in green; each component is plotted in blue; and the summed continuum is plotted in red. The middle panel shows the residual, pure emission-line spectrum. Two blue dashed lines mark the positions of Hβ $\lambda4861$ and [O III] $\lambda5007$. The bottom panel shows the spectrum after subtracting the power law and the Balmer continuum in the wavelength range 4100–5600 Å. The red spectrum is our Fe model. The blue dashed line in the bottom panel is the position of the peak of Fe II $\lambda4924$ with zero velocity shift.

tween input and output parameters can then be compared to evaluate potential systematic errors and biases.

We build the simulated continuum spectrum as a linear combination of a single power law and Fe emission expressed by Eq. (5). We generate a realistic noise pattern for the spectra using a real error array taken from SDSS observations, scaling it by a multiplicative factor to match the desired S/N of the simulation. For each pixel of the simulated spectrum, a Gaussian random deviation is added. Bad pixels have large deviates statistically. We use a mask array from an actual FITS file to locate the masked pixels; some of the pixels that have large errors are masked by the SDSS pipeline, but not all. This pro-

cedure ensures that the simulated spectra have a realistic noise level and noise pattern.

There are three main factors that can affect the measurements of V_{Fe} and FWHM$_{Fe}$: (1) the S/N of the spectrum; (2) the strength (EW) of the iron emission; and (3) the width (FWHM) of the iron lines. Our simulations demonstrate that the input value of V_{Fe} in the simulated spectrum has a very minimal effect on the systematic bias of the measured output values of V_{Fe} or FWHM$_{Fe}$, and so we neglect it from further consideration. We calculate EW$_{Fe} = F$(Fe II $\lambda4570$)$/F_{5100}$ where, in the present paper, F(Fe II $\lambda4570$) is the flux of the Fe II emission between 4434 and 4684 Å. Most of the quasars
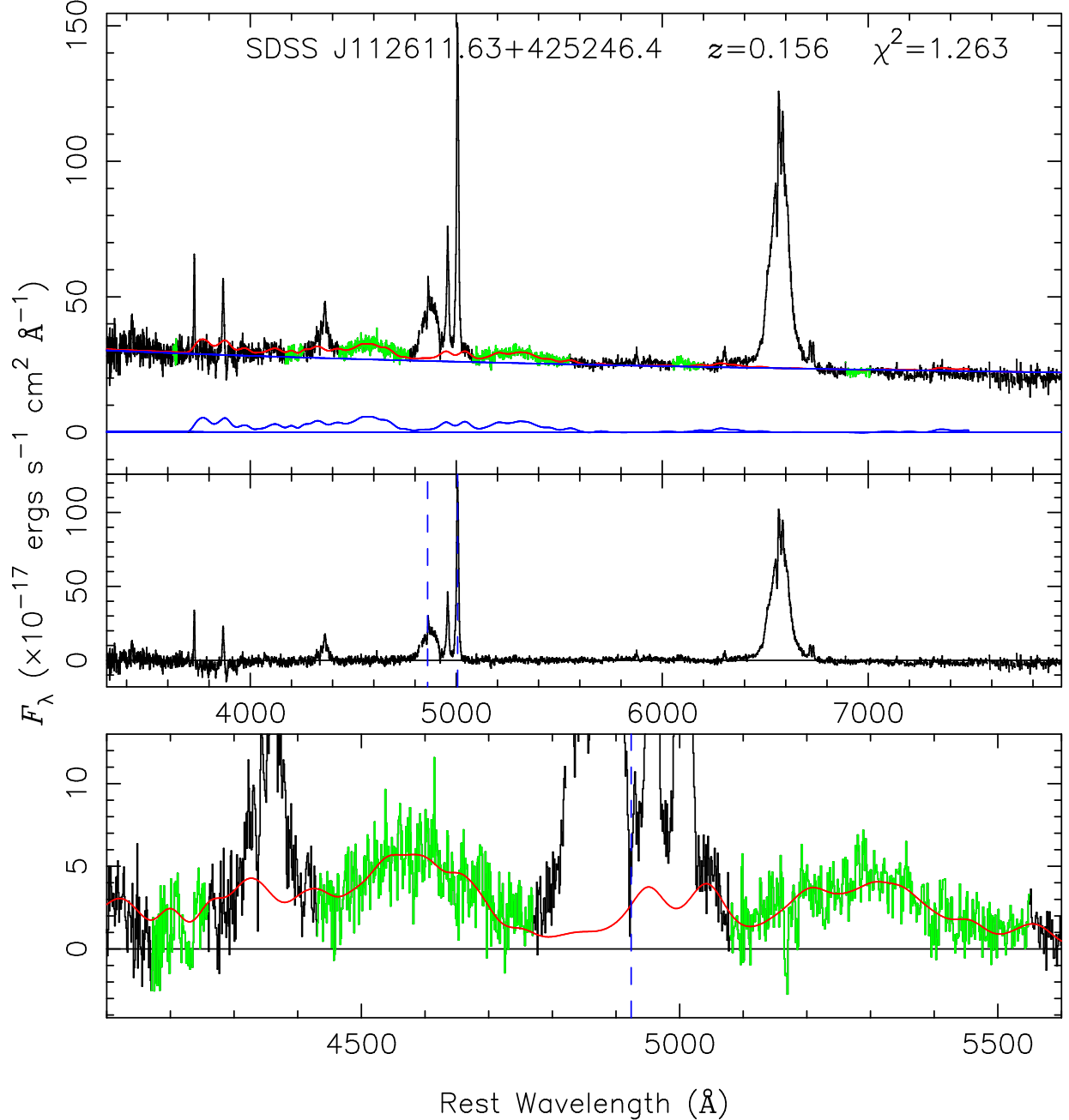
FIG. 2.— Same as Fig. 1, but for SDSS J112611.63+425246.4, which has broad Fe lines. Note the large departure of the modeled Fe II $\lambda4924$ line from its rest-frame wavelength (blue dashed line in the bottom panel). $v_{\rm Fe}$ is 1691 ± 119 km s^{-1}.

in the sample have a EW$_{\rm Fe}$ between 15 and 75 Å and FWHM$_{\rm Fe}$ between 1000 and 5000 km s^{-1}. Accordingly, we test four values of EW$_{\rm Fe}$ (15, 25, 50, 75 Å) and vary FWHM$_{\rm Fe}$ from 1000 to 5000 km s^{-1}, in steps of 500 km s^{-1}. We set S/N = 10, which is the lower limit of the S/N in the sample. $V_{\rm Fe}$ is fixed at zero so that we can examine whether the measured shifts are real or spurious.

For each pair of values for EW$_{\rm Fe}$ and FWHM$_{\rm Fe}$, we generate 100 spectra. We fit the continuum and then calculate the quantity

$$\delta_{\rm sim}^{V} = \frac{V_{\rm in} - V_{\rm out}}{{\rm FWHM}_{\rm in}}, \qquad (8)$$

where $V_{\rm in}$ and $V_{\rm out}$ are input and output values of $V_{\rm Fe}$, respectively, and FWHM$_{\rm in}$ is the input FWHM$_{\rm Fe}$. Figure 4a shows $\delta_{\rm sim}^{V}$ as a function of FWHM$_{\rm Fe}$. The results are plotted using

different colors and line styles for different values of EW$_{\rm Fe}$. For each EW$_{\rm Fe}$, there are three lines: the middle line represents the mean $\delta_{\rm sim}^{V}$, and the other two lines above and below are one standard deviations ($\sigma_{\rm sim}^{V}$) above and below the mean. From the diagram, we can see that the average value of $\delta_{\rm sim}^{V}$ is always close to 0. This demonstrates that the measured value of $V_{\rm Fe}$ shows no systematic redshift or blueshift with increasing FWHM$_{\rm Fe}$ and EW$_{\rm Fe}$. Obviously, $\sigma_{\rm sim}^{V}$ increases with decreasing EW$_{\rm Fe}$; measuring Fe II emission is very uncertain when EW$_{\rm Fe}$ is small. Based on the results of these tests, we decided to exclude from the sample sources with EW$_{\rm Fe}$ < 25 Å. It should be noted that the S/N in this particular simulation is set at the lower limit of our sample, so the uncertainties shown in Figure 4 should be considered upper limits. Figure 4b shows the difference between the error given by our
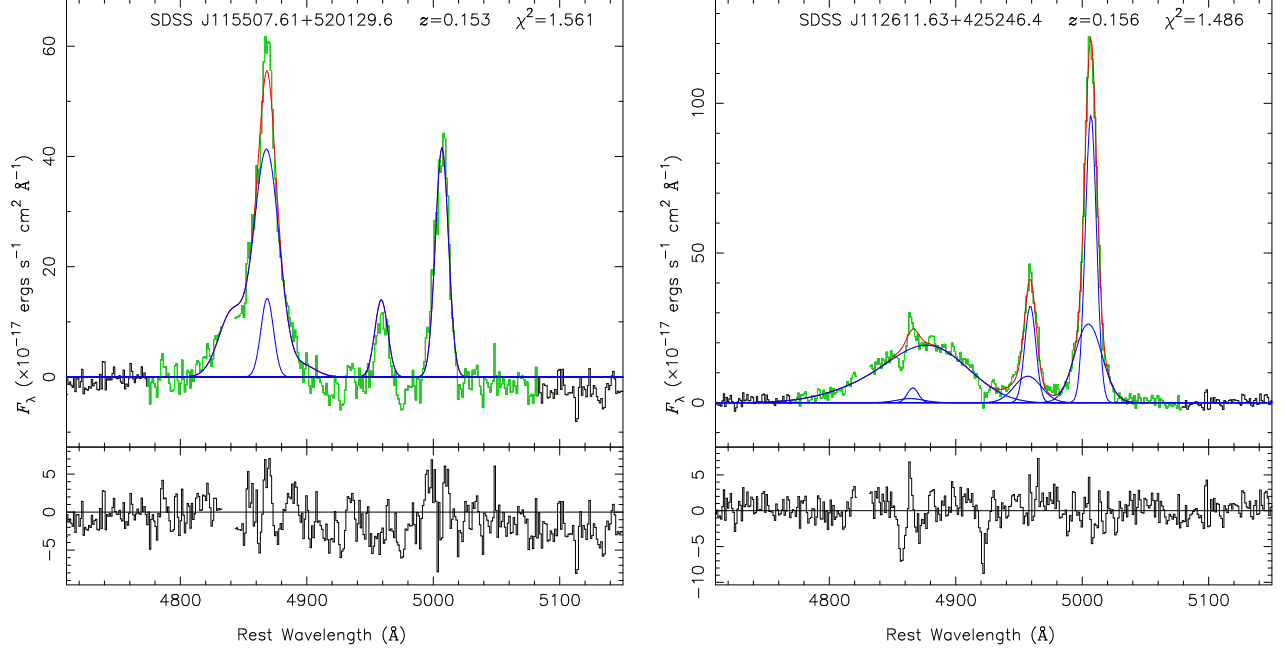
FIG. 3.— Fitting of the emission lines for the two quasars in Figs. 1 and 2. The top panel shows the pure emission-line spectrum. Each component is in blue, and the sum of them is in red. The bottom panel shows the residuals.

code and that given by the simulation. $\sigma_{\rm fit}^V$ is the average value of the errors given by the code in the 100 trials divided by FWHM$_{\rm in}$.

Figures 4c and 4d show the systematic error in the measurement of FWHM$_{\rm Fe}$. We define

$$\delta_{\rm sim}^{\rm FWHM} = \frac{\rm FWHM_{out}}{\rm FWHM_{in}} - 1. \qquad (9)$$

The standard deviation of $\delta_{\rm sim}^{\rm FWHM}$ is denoted by $\sigma_{\rm sim}^{\rm FWHM}$, and $\sigma_{\rm fit}^{\rm FWHM}$ is the average value of the relative errors of FWHM$_{\rm Fe}$ (defined as the error of the FWHM$_{\rm Fe}$ divided by FWHM$_{\rm in}$) given by the code.

From these simulations, we conclude: (1) the mean values of $\delta_{\rm sim}^V$ and $\delta_{\rm sim}^{\rm FWHM}$ cluster around 0 and exhibit no trend as a function of FWHM$_{\rm Fe}$ or EW$_{\rm Fe}$; (2) the error given by our code is consistent with that given by the simulations (except perhaps for the EW$_{\rm Fe}$ = 15 Å bin). These results show that our measurements are reliable and robust.

3.4. *Comparison with Conventional Fe Template-fitting Methods*

There are two conventional methods for Fe fitting. Both have been widely used and effective. The first (model 1) assumes that the Fe lines have no velocity shift but that their width can be different with that of H$\beta_{\rm BC}$ (e.g., Boroson & Green 1992; Marziani et al. 1996; McLure & Jarvis 2002; Dietrich et al. 2003; Greene & Ho 2005b; Kim et al. 2006; Woo et al. 2006). Alternatively (model 2), one assumes that the Fe lines have no shift and that they have the same width as H$\beta_{\rm BC}$ (e.g., Netzer & Trakhtenbrot 2007; Salviander et al. 2007). Two obvious questions arise. Does our continuum model (Eq. (1)) significantly improve the fit? And second, how does our continuum decomposition affect the emission-line measurements (e.g., Hβ and [O III]) and the physical parameters subsequently derived from them (e.g., central BH mass and the Eddington ratio)?

We compare the results derived from our approach with the two standard methods described above. Following Lupton

(1993, Chapter 12.1), we use the F-test[8] to calculate how significantly our model improves the fit for each source. Comparing with model 1, 71% of the sources are better fit by our model at a significance of >95.45%, and 58% of the sources are better fit at a significance level of >99.73%. With respect to model 2, the corresponding improvement can be seen in 89% of the sources at a significance of >95.45% and in 80% of the sources at a significance of >99.73%. On average, our model decreases the reduced χ^2 by 0.039 and 0.094 compared with models 1 and 2, respectively. We conclude that our approach of allowing $V_{\rm Fe}$ and FWHM$_{\rm Fe}$ to be free parameters significantly improves the fit in most objects.

Next, we evaluate the actual impact that the different methods have on measured and derived physical quantities. We measure the H$\beta_{\rm BC}$ and [O III] emission lines, derive $M_{\rm BH}$ and $L_{\rm bol}/L_{\rm Edd}$ (see §4.4) for each model, and then calculate the relative differences of the parameters between our model and the two fiducial standard models. As summarized in Table 1, the differences in line luminosities and line widths for H$\beta_{\rm BC}$ and [O III], $M_{\rm BH}$, and $L_{\rm bol}/L_{\rm Edd}$ are all less than 5%, while changes in velocity shifts are also no more than 50 km s^{-1}. The only exception is for sources with very weak [O III] lines. In this regime, the measurement of [O III] can be strongly affected by Fe II $\lambda4924$ and Fe II $\lambda5018$, and the effect on $L_{\rm [O III]}$ and FWHM$_{\rm [O III]}$ in Table 1 is large (a few tens of percent). This exercise demonstrates that, for most applications, the choice of method for Fe template fitting is in practice unimportant—unless the main scientific objective is to actually study the Fe II emission itself.

3.5. *Redshifts*

The narrow emission lines are commonly used to obtain the systemic redshift. The [O III] $\lambda5007$ line is the strongest narrow line for most quasars, so it is most often used. However, Boroson (2005) showed that [O III] can be blueshifted with

---

[8] Strictly speaking, this test is valid only for models that use linear fitting. But it has been empirically used for nonlinear models and seems to be effective (e.g., see Hao et al. 2005).
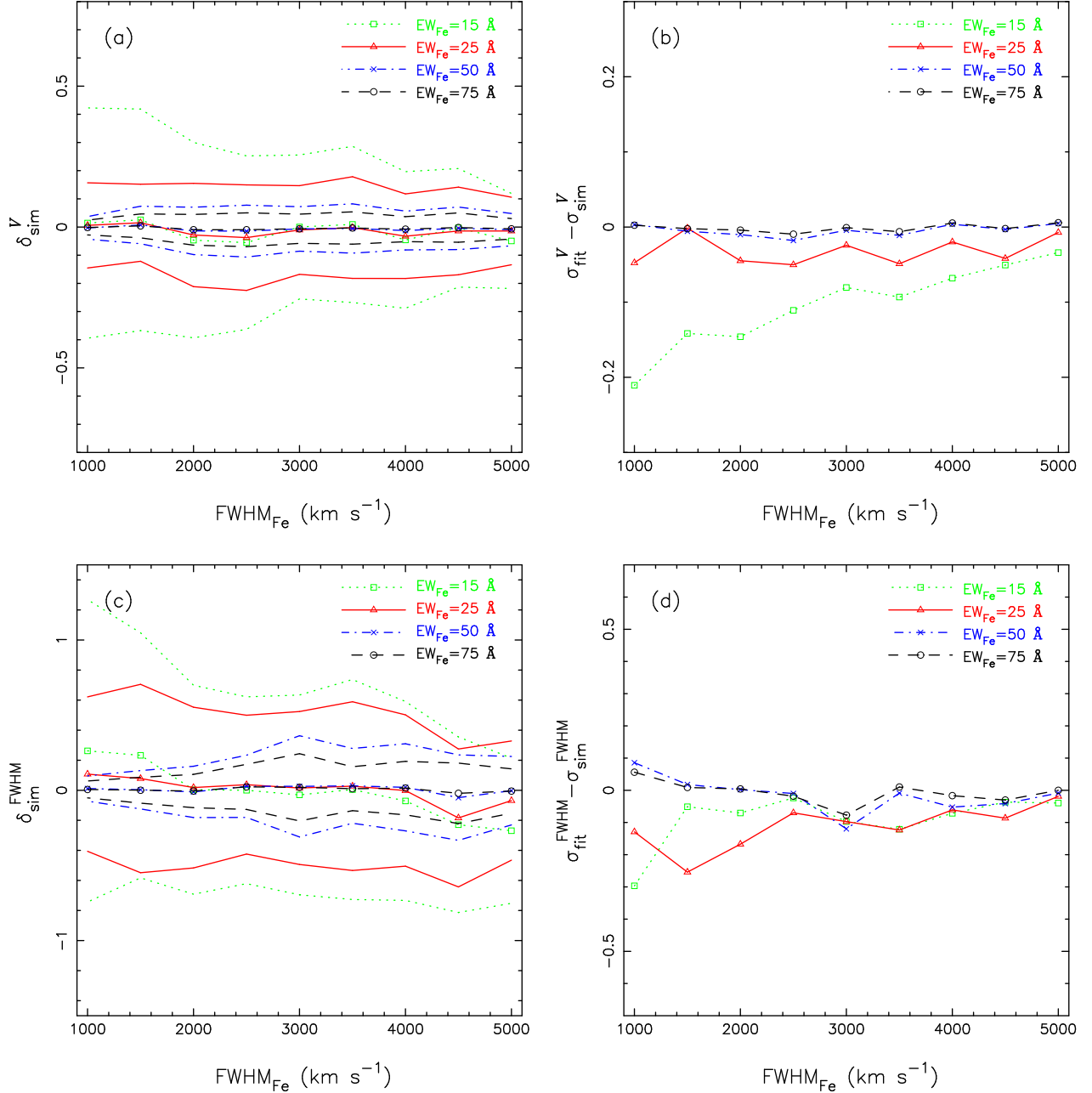
FIG. 4.— (a) Input-output simulations of v_{Fe} measurements. We define $\delta_{sim}^V = (V_{in} - V_{out})/FWHM_{in}$. For each EW_{Fe}, the middle line represents the mean δ_{sim}^V, and the other two lines above and below are one standard deviation above and below the mean. The S/N in the simulation is 10, which is the lower limit of our sample, so the uncertainties shown here should be considered upper limits. (b) Test of the error bars given by the code. σ_{fit}^V is the average value of the errors given by the code in 100 trials, divided by $FWHM_{in}$, and σ_{sim}^V is the standard deviation of δ_{sim}^V. (c) Input-output simulations of $FWHM_{Fe}$ measurements. We define $\delta_{sim}^{FWHM} = (FWHM_{out} - FWHM_{in})/FWHM_{in}$. (d) Test of the error bars by the code. σ_{fit}^{FWHM} is the average value of the relative errors of $FWHM_{Fe}$ given by the code in 100 trials, and σ_{sim}^{FWHM} is the standard deviation of δ_{sim}^{FWHM}. See text for details of the simulation.

TABLE 1
EFFECT OF FE TEMPLATE-FITTING METHOD ON OTHER PARAMETERS

Model (1)	$L(H\beta_{BC})$ (2)	$FWHM(H\beta_{BC})$ (3)	$V(H\beta_{BC})$ (4)	$L_{[O\,III]}$ (5)	$FWHM_{[O\,III]}$ (6)	$V_{[O\,III]}$ (7)	M_{BH} (8)	L_{bol}/L_{Edd} (9)
fix V_{Fe}, free $FWHM_{Fe}$	−1.75%(2.99%)	−1.74%(3.54%)	−27.2(49.2)	−2.15%(5.01%)	−1.02%(9.51%)	2.76(35.6)	−0.07%(0.49%)	2.23%(11.2%)
fix both V_{Fe} and $FWHM_{Fe}$	−1.46%(3.14%)	−0.39%(4.10%)	−23.2(47.9)	−0.48%(5.58%)	−0.31%(10.22%)	2.95(32.0)	−0.01%(0.46%)	0.63%(10.5%)

NOTE. — Changes in emission-line parameters and derived physical parameters due to using different Fe template-fitting models. Col. (2): luminosity of $H\beta_{BC}$. Col. (3): FWHM of $H\beta_{BC}$. Col. (4): $H\beta_{BC}$ velocity shift. Col. (5): luminosity of [O III]. Col. (6): FWHM of [O III]. Col. (7): [O III] velocity shift. Col. (8): mass of the central BH. Col. (9): Eddington ratio of the central BH (see §4.4 for details of how to derive M_{BH} and L_{bol}/L_{Edd}). Each column shows the relative changes in percentage, except for Col. (4) and (7), which show the difference in absolute velocity shift in km s^{-1}. The number in parenthesis is the standard deviation.
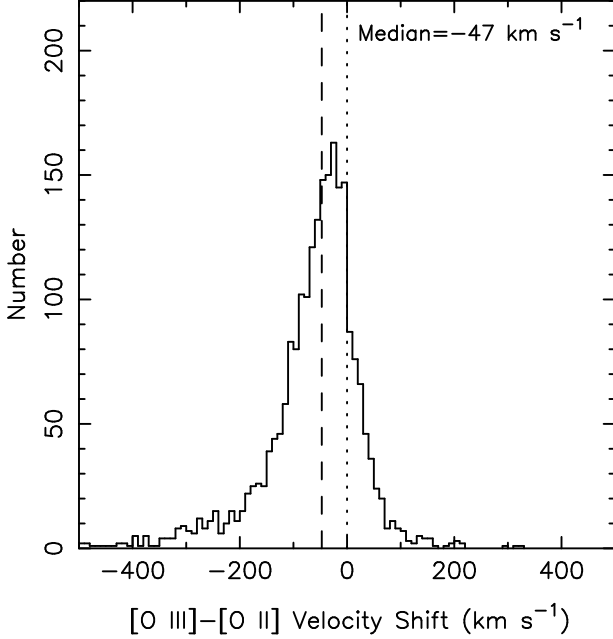
FIG. 5.— Distribution of [O III] velocity shifts with respect to [O II]. Positive velocity indicates a redshift. The dotted line marks the position of zero velocity shift, while the dashed line marks the median of the distribution.

respect to the low-ionization forbidden lines, which provide a better rest-frame. In our sample, 2265 sources ($\sim 50\%$) have detectable [O II] $\lambda 3727$ emission. Figure 5 shows the distribution of velocity shifts between [O III] and [O II]; positive velocity indicates a redward shift. Consistent with the results of Boroson (2005), the majority of the sources have blueshifted [O III]; the median blueshift is -47 km s^{-1}. Because the [O III] blueshifts are much smaller than the velocity shifts seen in Fe II and in other broad lines (see §4.1) and only half of our sample is detected in [O II], we still use [O III] to define the rest-frame. Thus, we define the Fe II velocity shift by $v_{Fe} = V_{Fe} - V_{[O III]}$, where $V_{[O III]}$ is the velocity shift of the core component of the [O III] $\lambda 5007$ line measured in §3.2.

3.6. Errors

We calculate the error of v_{Fe} from the fitting of the continuum and the fitting of the [O III] line. Figure 6a shows the distribution of the v_{Fe} errors. Most velocity shifts have an error < 200 km s^{-1}, and the median of the distribution is 116 km s^{-1}. We also plot the relative error on FWHM$_{Fe}$ in Figure 6b. The typical value is about 10% to 20%, and the median is 12.0%.

4. RESULTS

The full catalog of the measurements used in the analysis below is available electronically. Table 2 describes the contents and the formats of each column. All the emission line velocity shifts are with respect to [O III] $\lambda 5007$ and a positive value indicates a redward shift. -9999 in the columns of Mg II (Col. 21—26) and [O II] (Col. 35—40) measurements indicates the line lies out of the SDSS spectral coverage or too weak to be detected (see §3.2 for details). The details of how to deriving the radio and X-ray properties (Col. 19 & 20), and the M_{BH} and Eddington ratio L_{bol}/L_{Edd} (Col. 42 & 43), are described in §4.5 and §4.4 respectively.

4.1. Fe Emission Shifts

From the distribution of v_{Fe} (Fig. 7a), we can clearly see that most quasars exhibit Fe II emission that is *redshifted* with respect to the systemic velocity of the narrow-line region (defined by [O III]). Only 481 out of 4037 quasars have blueshifts. The median shift is $v_{Fe} = +407$ km s^{-1} (the vertical dashed line in the figure), with a maximum value of $v_{Fe} \approx 2000$ km s^{-1}. Considering that the typical error on v_{Fe} is only <200 km s^{-1} (§3.6), the vast majority of the values in the redshifted tail of the v_{Fe} distribution must be real. For comparison, we also calculate the distribution of Fe II velocity shift with respect to [O II] (Fig. 7b). The results obtained by using [O II] as reference instead of [O III] are very similar and lead to the same conclusion.

To rule out the possibility that the excess Fe II redshifts arise from artifacts due to poor data quality or fitting errors, we examined a subset of data using the much stricter selection criteria that S/N > 15 and $\chi^2 < 1.2$. These 309 quasars have the best data quality and the most reliable continuum fitting. The shape of the distribution of v_{Fe} this subsample (Fig. 7c) is quite similar to that of our whole sample. The median velocity shift is 414 km s^{-1}. We conclude on the basis of this test, as well as the Monte Carlo simulations described in §3.3, that the Fe II redshifts are robust and reliable.

Finally, we illustrate that the velocity shifts found for Fe II really do imply radial motions of the Fe II-emitting region, and not others. Figures 7d and 7e show the velocity shifts for Hβ_{BC} [v(Hβ_{BC})] and Mg II. The distribution of v(Hβ_{BC}) is almost symmetrical around 0, with a median value of only 65 km s^{-1} and a maximum value of about ± 1000 km s^{-1}. This result is consistent with previous studies (e.g., Fig. 3 of Sulentic et al. 2000a; Fig. 2 of Baskin & Laor 2005; Fig. 6 of Shang et al. 2007). Most recently, Bonning et al. (2007) also studied the velocity shift of Hβ_{BC} using SDSS quasars, and our result is very similar to theirs; they fit their distribution of velocity shifts (their Fig. 1) using a Gaussian profile with a peak velocity of 100 km s^{-1}. Our distribution of Mg II shifts is indistinguishable from that of Hβ_{BC}. It is symmetrical around 0, has a median value of 113 km s^{-1} and a maximum value of about ± 1000 km s^{-1}, and it is consistent with those given in, for example, Richards et al. (2002b) and Shang et al. (2007).

In order to compare Fe II directly with Hβ_{BC}, we also plot the distribution of the Fe II velocity shift with respect to Hβ_{BC}, as shown in Figure 7f. Again, most objects have redward shifts in Fe II.

4.2. Fe Emission Widths

Figures 8a and 8b show the distribution of FWHM$_{Fe}$ and FWHM(Hβ_{BC}), respectively. FWHM$_{Fe}$ has an artifical lower limit of 900 km s^{-1}, which is bounded by the I Zw 1 Fe II template. The median value of FWHM$_{Fe}$, 2533 km s^{-1}, is ~ 0.74 of that of FWHM(Hβ_{BC}) (3445 km s^{-1}). Almost all the sources have Fe II lines narrower than Hβ_{BC}, and the majority have FWHM$_{Fe} \approx 3/4$ FWHM(Hβ_{BC}) (Fig. 8c). This result is contrary to the prevailing notion that Fe II and Hβ_{BC} have similar profiles and are emitted from the same region (e.g., Boroson & Green 1992), but is consistent with some more recent studies of a few objects (e.g., Popović et al. 2007; Matsuoka et al. 2008).

We find that FWHM(Hβ) and FWHM(Mg II) are well correlated and roughly equal (Fig. 8d), consistent with McLure & Jarvis (2002); Salviander et al. (2007). Salviander et al. (2007) find that FWHM(Hβ) tends to be larger than FWHM(Mg II) for FWHM(Hβ) > 4000 km s^{-1}, an effect they attribute to an extensive red wing on Hβ. This
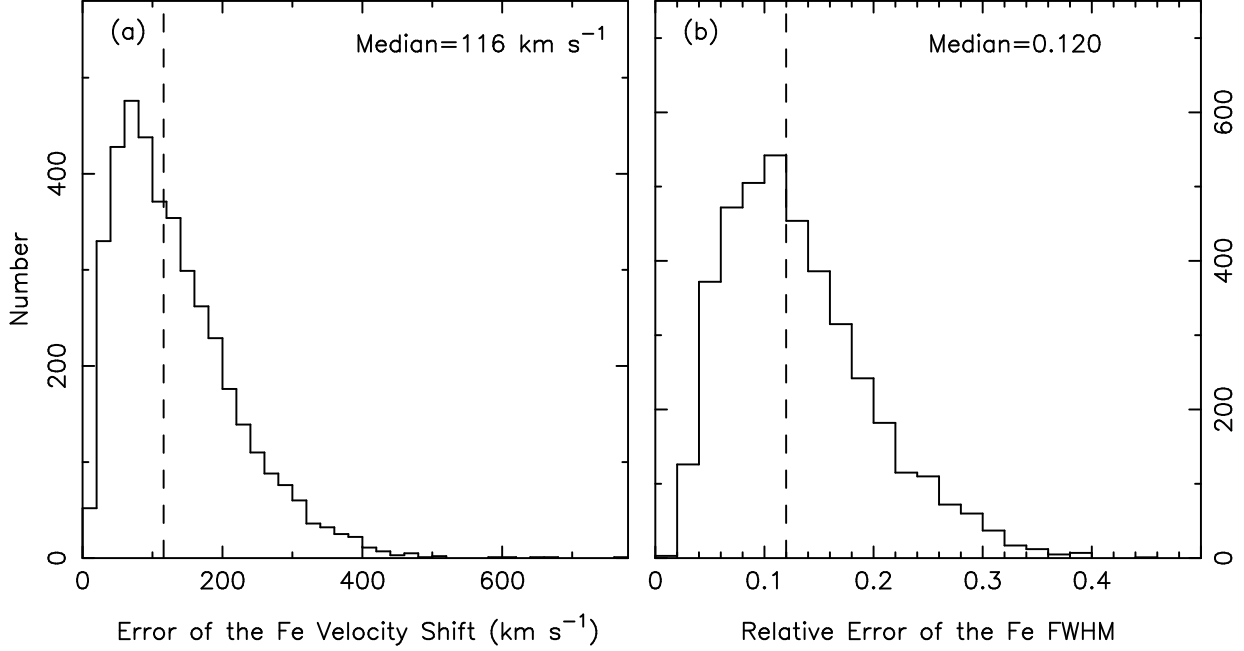
FIG. 6.— Distribution of (*a*) error in the Fe II velocity shift and (*b*) relative error in Fe II FWHM. The dashed line marks the median of the distribution.

tendency can also be seen in our plot, and our composite spectra (Fig. 13) do show that Hβ tends to have a red asymmetry when broad.

4.3. *Correlations with Other Emission-line Parameters*

Boroson & Green (1992) used principal components analysis to study the correlations among various observed properties of nearby quasars, and found that most of the variance in the optical spectra of quasars is connected with the inverse correlation between Fe II and [O III] strength. The soft X-ray photon index (Γ_{soft}), the ratio of Fe II to Hβ_{BC} (R_{Fe}), and the line width of Hβ_{BC} [FWHM(Hβ_{BC})] correlate with each other (Boller et al. 1996; Wang et al. 1996; Laor et al. 1997a). Sulentic et al. (2000a,b, 2007) identified that FWHM(Hβ_{BC}), R_{Fe}, Γ_{soft}, and the velocity shift at half maximum of the broad C IV line profile [$c(\frac{1}{2})$] provide discrimination between different AGN types. So, for simplicity, instead of using a formal principal components analysis to study the correlations between Fe II and other parameters, we just study the correlations with FWHM(Hβ_{BC}) and R_{Fe}.

The left panel of Figure 9 shows the dependence of v_{Fe} on FWHM(Hβ_{BC}) for our sample. The crosses in the figure present the median values of the errors in both coordinates. Dividing the sample by a vertical line of FWHM(Hβ_{BC}) = 3000 km s^{-1} and a horizontal line of v_{Fe} = 800 km s^{-1}, we find that almost all sources with FWHM(Hβ_{BC}) < 3000 km s^{-1} have v_{Fe} < 800 km s^{-1}, and most sources with v_{Fe} > 800 km s^{-1} have FWHM(Hβ_{BC}) > 3000 km s^{-1}. Sources with large v_{Fe} and low FWHM(Hβ_{BC}) are rare. There is also a large spread in v_{Fe} for sources with FWHM(Hβ_{BC}) > 3000 km s^{-1}. Note that narrow-line Seyfert 1 galaxies (NLS1s), defined by FWHM(Hβ_{BC})< 2000 km s^{-1} (Osterbrock & Pogge 1985), almost all have low v_{Fe} in our sample.

Following Netzer & Trakhtenbrot (2007), we define R_{Fe} as the line luminosity ratio of Fe II and Hβ_{BC},

$$R_{\mathrm{Fe}} = \frac{L(\text{Fe II } \lambda 4570)}{L(\text{H}\beta_{\mathrm{BC}})}, \qquad (10)$$

where L(Fe II λ4570) is the luminosity of Fe II emission be-

tween λ4434 and λ4684. The right panel of Figure 9 shows the correlation diagram for v_{Fe} versus R_{Fe}. The vertical line is R_{Fe} = 1. Most sources with R_{Fe} > 1 have small v_{Fe}. Sources with large R_{Fe} and large v_{Fe} are rare. This correlation agrees with the correlation between R_{Fe} and $L_{\mathrm{bol}}/L_{\mathrm{Edd}}$ shown in Figure 5 of Netzer & Trakhtenbrot (2007), considering the strong inverse correlation between v_{Fe} and $L_{\mathrm{bol}}/L_{\mathrm{Edd}}$ as we find in §4.4, below.

The statistical connection between v_{Fe} and FWHM(Hβ_{BC}) or R_{Fe} is similar to those shown in Figures 2 and 9 of Boroson & Green (1992). This suggests that v_{Fe} can also provide useful empirical discrimination between different types of AGNs from optical spectra.

4.4. *The Physical Driver of v_{Fe}*

The Eddington ratio $L_{\mathrm{bol}}/L_{\mathrm{Edd}}$ is often suggested to be the main physical driver of the spectral diversity in quasars (Sulentic et al. 2000a,b; Marziani et al. 2001; Boroson 2002; Marziani et al. 2003a), and M_{BH} is argued to be an important determinant of radio-loudness (Laor 2000; Boroson 2002; McLure & Jarvis 2004, but see Ho 2002). This section investigates attempts to determine which physical variable is the main driver of variations in v_{Fe}.

Central black hole masses can be estimated from empirical relations derived from reverberation mapping. We derived the BH mass and $L_{\mathrm{bol}}/L_{\mathrm{Edd}}$ using the relation calibrated by McGill et al. (2008),

$$\log\left(\frac{M_{\mathrm{BH}}}{M_{\odot}}\right) = 7.383 + 2\log\left(\frac{\sigma_{\mathrm{H}\beta}}{1000 \text{ km s}^{-1}}\right)$$
$$+ 0.69\log\left(\frac{\lambda L_{5100}}{10^{44} \text{ ergs s}^{-1}}\right) \qquad (11)$$

(their Table 3; we use the factors for $L_{5100,t}$ and $\sigma_{\mathrm{H}\beta}$). We estimate the bolometric luminosity using $L_{\mathrm{bol}} = 9\lambda L_{5100}$ (Kaspi et al. 2000).

Figure 10*a* shows v_{Fe} as a function of $L_{\mathrm{bol}}/L_{\mathrm{Edd}}$ for our sample. The vertical dot-dashed line is $\log(L_{\mathrm{bol}}/L_{\mathrm{Edd}})$ = −0.8, and the horizontal dot-dashed line is v_{Fe} = 800 km s^{-1}. We
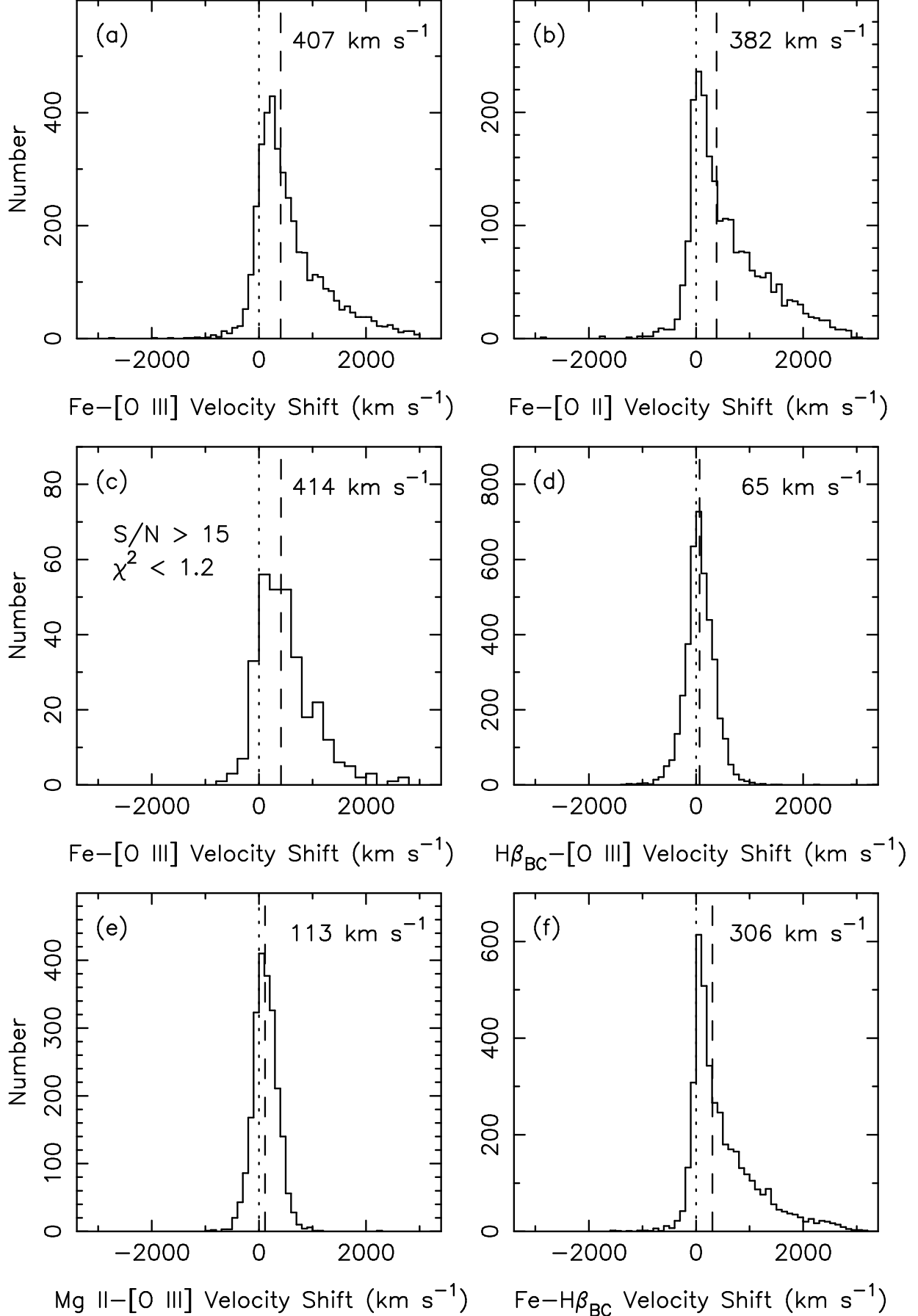
FIG. 7.— (*a*) Distribution of Fe II velocity shifts with respect to [O III]. (*b*) Fe II velocity shifts with respect to [O II]. Panel (*c*) shows the distributions of v_{Fe} in the subsample that has stricter criteria S/N > 15 and χ^2 < 1.2. (*d*) Hβ_{BC} velocity shifts with respect to [O III]. (*e*) Mg II velocity shifts with respect to [O III]. (*f*) Distribution of Fe II velocity shifts with respect to Hβ_{BC}. Positive velocity indicates a redshift. The number in each panel is the median value of the respective distribution, which is also marked by the dashed line. The dotted line marks the position of zero velocity shift.

TABLE 2
Spectrophotometric Measurements Table Format

| Column	Format	Units	Label	Description
1	a18	$\cdots$	SDSS Name	SDSS DR5 Object Designation hhmmss.ss+ddmmss.s (J2000.0)
2	f8.4	$\cdots$	z	Redshift determined using the peak of the [O III] $\lambda 5007$
3	e12.4	ergs s^{-1}	L(Fe II $\lambda 4570$)	Luminosity of the Fe II emission between 4434 and 4686 Å
4	e12.4			Error in L(Fe II $\lambda 4570$)
5	f8.1	km s^{-1}	FWHM$_{Fe}$	Fe II FWHM
6	f8.1			Error in FWHM$_{Fe}$
7	f8.1	km s^{-1}	v_{Fe}	Fe II velocity shift; all the emission line velocity shifts are with respect to [O III] $\lambda 5007$, and a positive value indicates a redward shift.
8	f8.1			Error in v_{Fe}
9	e12.4	ergs s^{-1}	$L(H\beta_{BC})$	Hβ_{BC} luminosity
10	e12.4			Error in $L(H\beta_{BC})$
11	f8.1	km s^{-1}	FWHM(Hβ_{BC})	Hβ_{BC} FWHM
12	f8.1			Error in FWHM(Hβ_{BC})
13	f8.1	km s^{-1}	v(Hβ_{BC})	Hβ_{BC} velocity shift
14	f8.1			Error in v(Hβ_{BC})
15	e12.4	ergs s^{-1} $^{-1}$	L_{5100}	Specific continuum luminosity at 5100 Å
16	e12.4			Error in L_{5100}
17	f7.3	$\cdots$	α	Power law spectral index of the continuum
18	f7.3	$\cdots$		Error in α
19	a2e10.3	ergs s^{-1} Hz^{-1}	L_{6cm}	Specific luminosity at 6 cm derived from the Peak flux density measured in FIRST, assuming a radio spectral index = -0.5; the upper limits are derived from the FIRST flux limits; -1.000 indicates not in FIRST survey area.
20	e11.3	ergs s^{-1} Hz^{-1}	L_{2keV}	Specific luminosity at 2 kev derived from *ROSAT* PSPC count rate; 0.000 means no detection.
21	e12.4	ergs s^{-1}	$L_{Mg\,II}$	Mg II luminosity; -9999 means no detection.
22	e12.4			Error in $L_{Mg\,II}$
23	f8.1	km s^{-1}	FWHM$_{Mg\,II}$	Mg II FWHM
24	f8.1			Error in FWHM$_{Mg\,II}$
25	f8.1	km s^{-1}	$v_{Mg\,II}$	Mg II velocity shift
26	f8.1			Error in $v_{Mg\,II}$
27	e12.4	ergs s^{-1}	$L_{[O\,III]}$	[O III] $\lambda 5007$ luminosity
28	e12.4			Error in $L_{[O\,III]}$
29	f8.1	km s^{-1}	FWHM$_{[O\,III]}$	[O III] $\lambda 5007$ FWHM
30	f8.1			Error in FWHM$_{[O\,III]}$
31	e12.4	$\cdots$	$L(H\beta_{NC})/L_{[O\,III]}$	Ratio of Hβ_{NC} to [O III] $\lambda 5007$
32	e12.4	$\cdots$		Error in $L(H\beta_{NC})/L_{[O\,III]}$
33	f8.1	km s^{-1}	v(Hβ_{NC})	Hβ_{NC} velocity shift
34	f8.1			Error in v(Hβ_{NC})
35	e12.4	ergs s^{-1}	$L_{[O\,II]}$	[O II] luminosity; -9999 means no detection.
36	e12.4			Error in $L_{[O\,II]}$
37	f8.1	km s^{-1}	FWHM$_{[O\,II]}$	[O II] FWHM
38	f8.1			Error in FWHM$_{[O\,II]}$
39	f8.1	km s^{-1}	$v_{[O\,II]}$	[O II] velocity shift
40	f8.1			Error in $v_{[O\,II]}$
41	f8.1	km s^{-1}	$\sigma_{H\beta}$	Square root of the second moment of Hβ_{BC}
42	e11.3	$M_{\odot}$	M_{BH}	Mass of the central Black Hole
43	e11.3	$\cdots$	L_{bol}/L_{Edd}	Ratio of bolometric luminosity to Eddtington luminosity
44	e12.4	$\cdots$	R_{Fe}	Ratio of Fe II to Hβ_{BC}
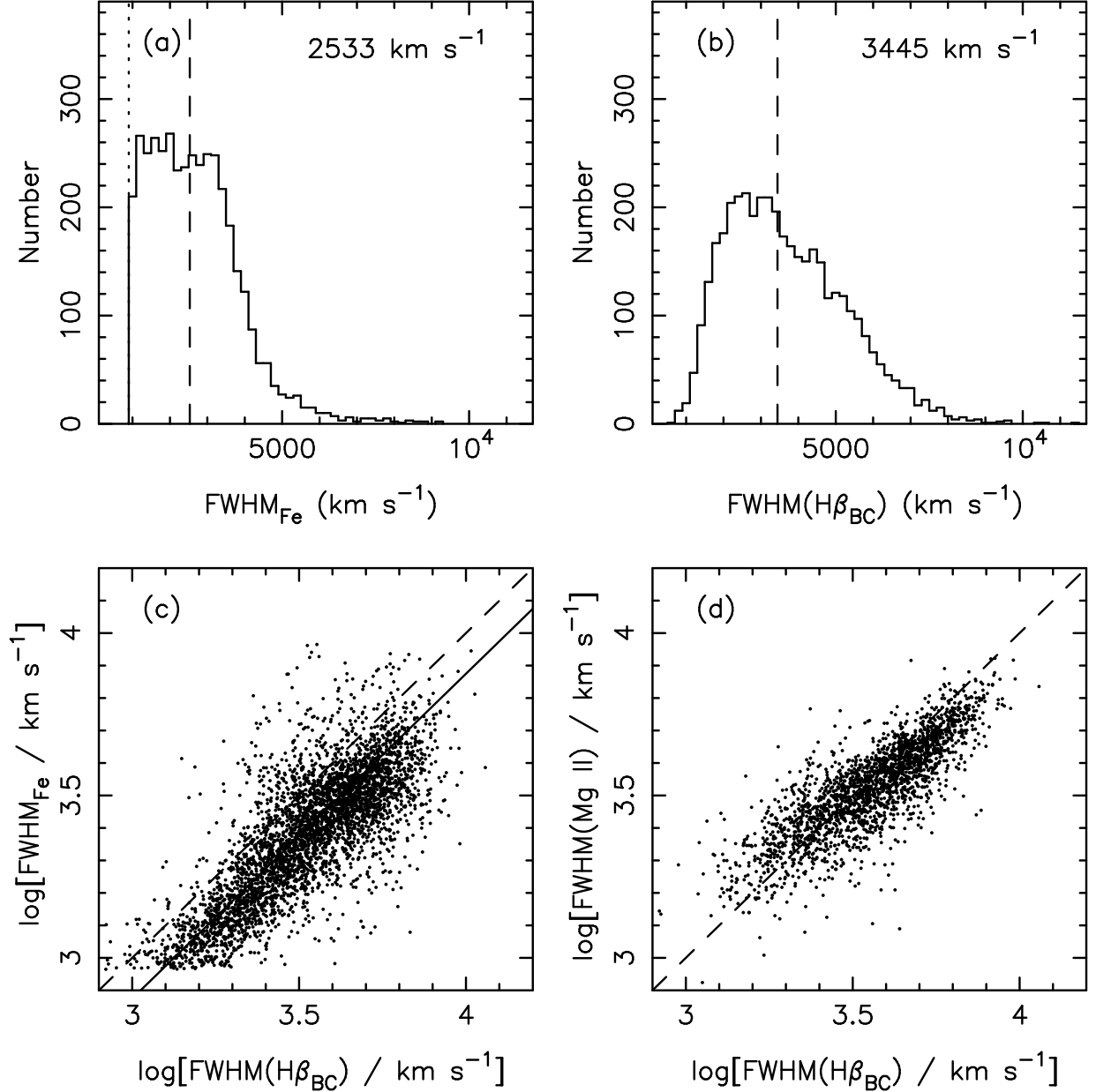
FIG. 8.— Distribution of (a) Fe II FWHM and (b) Hβ_{BC} FWHM. The number in the panel is the median FWHM, which is also marked by the dashed line. FWHM$_{Fe}$ has a lower limit of 900 km s^{-1} (dotted line); this is artificial because the I Zw 1 Fe template we used has a width of 900 km s^{-1}. (c) Correlation between FWHM$_{Fe}$ and FWHM(Hβ_{BC}). The dashed diagonal line shows FWHM$_{Fe}$ = FWHM(Hβ_{BC}), and the solid line is FWHM$_{Fe}$ = 3/4 FWHM(Hβ_{BC}). (d) Correlation between FWHM$_{Fe}$ and FWHM(Mg II). The dashed diagonal denotes FWHM(Hβ_{BC}) = FWHM(Mg II).

find that almost all sources with $\log(L_{bol}/L_{Edd}) > -0.8$ have $v_{Fe} < 800$ km s^{-1}, and most sources with $v_{Fe} > 800$ km s^{-1} have $\log(L_{bol}/L_{Edd}) < -0.8$. There are very few sources with large v_{Fe} and large L_{bol}/L_{Edd}. The error in L_{bol}/L_{Edd} is roughly 0.3 dex, which is dominated by the systematical error in estimating the BH mass using empirical relations (McGill et al. 2008).

The logarithmic form of this diagram is plotted in Figure 10b, excluding the 481 sources with negative v_{Fe}. We find a strong inverse correlation between v_{Fe} and L_{bol}/L_{Edd}. The fit taken into account the uncertainties in both quantities yields the solid line:

$$\log v_{Fe} = (1.00 \pm 0.05) - (1.83 \pm 0.05)\log(L_{bol}/L_{Edd}). \quad (12)$$

Pearson's correlation coefficient r_P is −0.53, and the probability P of a chance correlation $< 1 \times 10^{-5}$. Note that below

an v_{Fe} of about 150 km s^{-1}, the scatter to the fitted line increases. As mentioned in §3.3, the input value of V_{Fe} affects the measurements little; this means that the errors of v_{Fe} will not decrease with v_{Fe}. Thus, for sources with small v_{Fe}, the fractional error on v_{Fe} will be large. This causes the scatter described before. The squares show the mean values of $\log(L_{bol}/L_{Edd})$ in bins of $\Delta v_{Fe} = 200$ km s^{-1}; the error bars in panel (a) show the standard deviations. The dashed line shows the fit to the binned values of $\log(L_{bol}/L_{Edd})$:

$$\log v_{Fe} = (0.60 \pm 1.40) - (2.22 \pm 0.99)\log(L_{bol}/L_{Edd}) , \quad (13)$$

In this case, $r_P = -0.98$ and $P < 1 \times 10^{-5}$. The above analysis indicates that v_{Fe} depends strongly on L_{bol}/L_{Edd}; $v_{Fe} \propto (L_{bol}/L_{Edd})^{\gamma}$, with $\gamma \approx -2$: the larger the Eddington ratio, the lower the velocity shift v_{Fe}. Plotting v_{Fe} as an function of M_{BH} and L_{bol} (not shown) reveals that neither of these
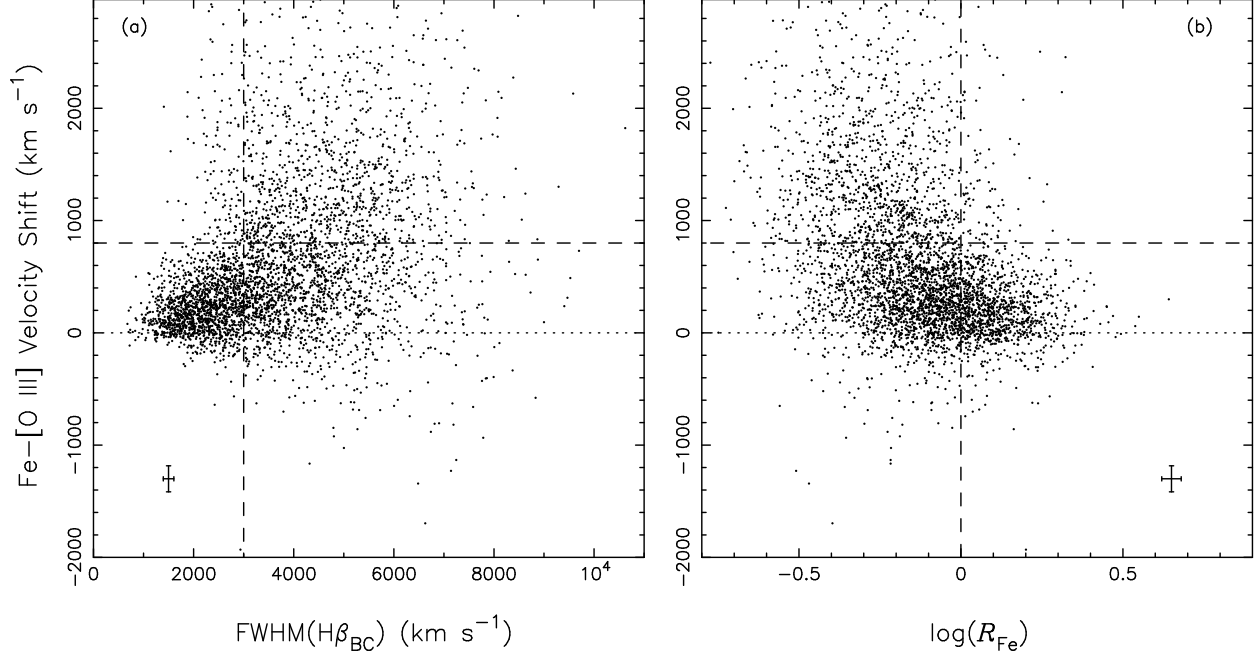
FIG. 9.— Correlation diagram for (*left*) $v_{\rm Fe}$ vs. FWHM(H$\beta_{\rm BC}$) and for (*right*) $v_{\rm Fe}$ vs. $R_{\rm Fe}$. The crosses in the figure present the median values of the errors in both coordinates. See text for description of the vertical and horizontal lines.
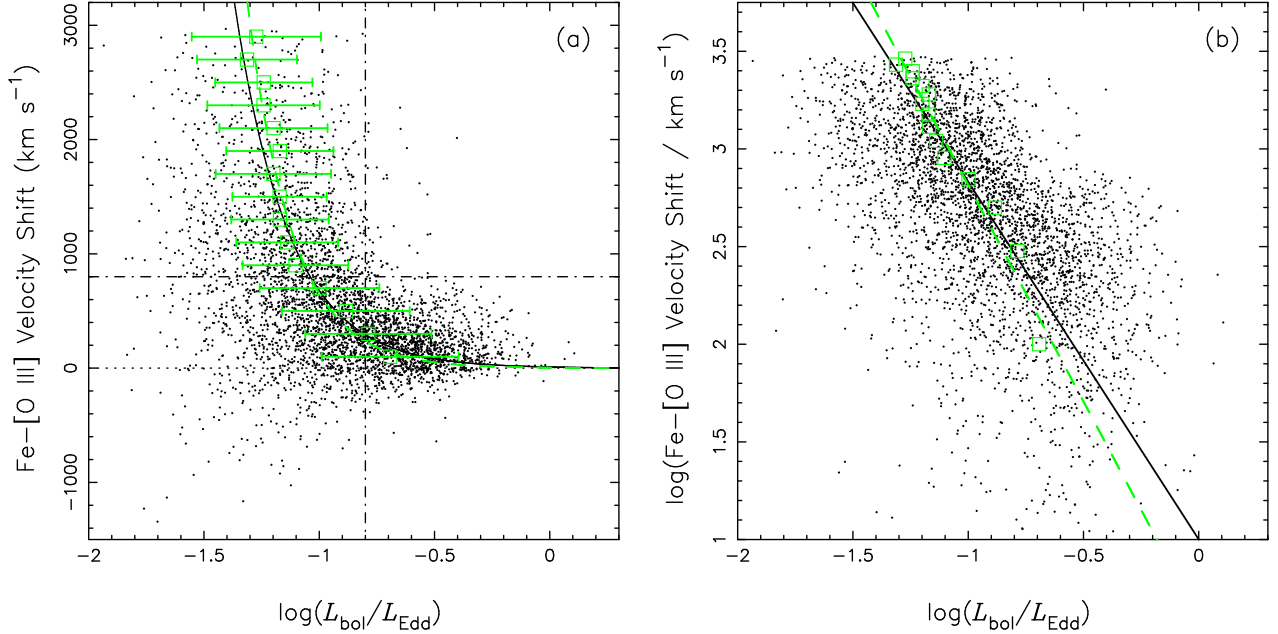

FIG. 10.— Correlation of Fe II velocity shift vs. Eddington ratio, with the Fe II velocity shift plotted (*a*) linearly and (*b*) logarithmically. See text explanation of the dot-dashed lines. The solid lines is the fit to data in Eq. (12). The green squares represent the mean $\log(L_{\rm bol}/L_{\rm Edd})$ in bins of $\Delta v_{\rm Fe} = 200$ km s^{-1}, and the error bars represent the standard deviations. The green dashed line shows the fit to the binned data.

two variables is as important as $L_{\rm bol}/L_{\rm Edd}$. The Eddington ratio is the main physical driver for $v_{\rm Fe}$. This result provides a strong constraint on theoretical models of the Fe II emission region.

4.5. *Correlations with Radio and X-ray Properties*

In an effort to understand the physical origin of the Fe II velocity shift, we examine whether $v_{\rm Fe}$ correlates with radio and X-ray emission. Richards et al. (2002b) conducted a similar investigation in their analysis of velocity shifts for the C IV line. Figure 11 (upper panel) plots the fraction of radio-loud quasars in bins of different $v_{\rm Fe}$. We define the radio-

loudness parameter as $R = \log(L_{\rm 6cm}/L_B)$, where $L_{\rm 6cm}$ and L_B are the observed luminosities at 6 cm and 4400 Å. We use the FIRST (Becker et al. 1995) peak flux densities at 20 cm in Table 2 of Schneider et al. (2007) to calculate the radio luminosity, assuming a radio spectral index $\alpha_{\rm r} = -0.5$. The optical luminosities are calculated from the power-law continuum we fitted. We classify the sources with $R > 1$ as radio-loud. There are a total of 165 radio-loud quasars out of 3750 sources in the present sample within the FIRST survey area. Note that the percentage of radio-loud quasars in our sample is $165/3750 = 4.4\%$, slightly lower than the 6.7% found by McLure & Jarvis (2004). The reason is probably that our
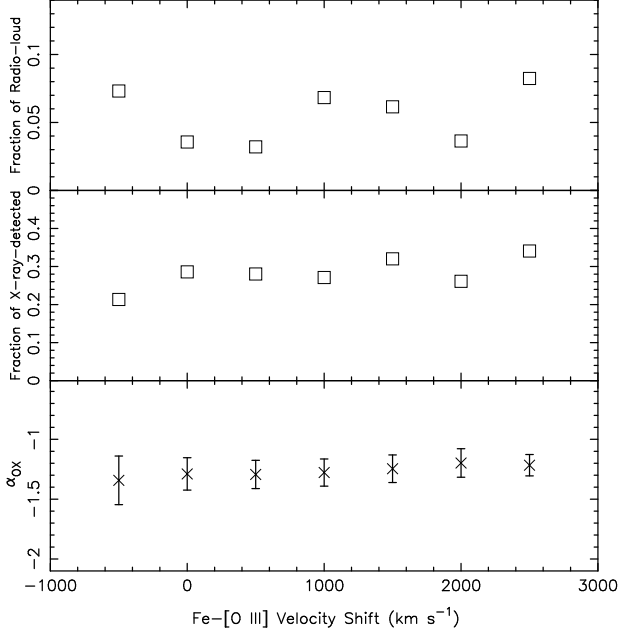
FIG. 11.— (*Top*) The fraction of radio-loud quasars in bins of different v_{Fe}. (*Middle*) The fraction of X-ray-detected quasars. (*Bottom*) α_{OX} in bins of different v_{Fe}.

sample is biased toward quasars with high L_{bol}/L_{Edd} (by our Fe II EW cut), since R decreases with increasing L_{bol}/L_{Edd} (Ho 2002; Greene et al. 2006). The rightmost bin have the largest radio-loud fraction, in which there are 7 radio-loud quasars out of 85, a fraction $\sim$2 times higher than average. The cumulative Poisson probability (P) of getting 7 or more objects out of 85 is 8.54×10^{-2} (Gehrels 1986) when the average is 3.74 ($165/3750 \times 85$), no more than a 3σ significance ($1 - P < 99.73\%$). Thus there is no clear trend of radio-loud fraction with v_{Fe}.

Next, we evaluate the fraction of X-ray-detected quasars as a function of v_{Fe} (middle panel of Fig. 11). We use the data from Schneider et al. (2007), who provide the X-ray full-band count rate from the *ROSAT* All-Sky Survey Bright (Voges et al. 1999) and Faint (Voges et al. 2000) sources catalogs. No obvious trend is apparent. Finally, we test for possible dependence of v_{Fe} on the optical-to-X-ray spectral index $\alpha_{OX} \equiv -0.3838 \log(L_{2500}/L_{2\,keV})$, where L_{2500} is the specific luminosity at 2500 Å calculated using the power-law continuum we measured and $L_{2\,keV}$ is the specific luminosity at 2 keV derived from the *ROSAT* count rate using PIMMS (Mukai 1993) assuming a power-law model with photon index of 2. We see no obvious trend between α_{OX} and v_{Fe} either (bottom panel of Fig. 11).

4.6. *Composite Spectra*

In order to get a visual impression of the correlations between v_{Fe} and other emission-line properties, we create a set of five composite spectra by combining quasars in bins of different v_{Fe}. We divide our sources into five subsamples, covering the following velocity ranges: -250 to 250 km s^{-1} (A, 1350 objects), 250 to 750 km s^{-1} (B, 1362 objects), 750 to 1250 km s^{-1} (C, 590 objects), 1250 to 1750 km s^{-1} (D, 332 objects), and 1750 to 2250 km s^{-1} (E, 180 objects). The composite spectra are generated following the procedure of Vanden Berk et al. (2001). The spectra of quasars in each subsample are deredshifted using the redshifts determined from [O III] and then normalized to unity average flux density over

the rest wavelength interval 5090–5110 Å. We generate the composites using the geometric mean, which is appropriate for quasars with power-law spectra because the geometric mean will result in a power law with the mean spectral index (Vanden Berk et al. 2001).

Figure 12 shows the composite spectra of the five subsamples described above. We plot the spectra in different colors and shifted them slightly vertically for clarity. The spectra are arranged so that, from top to bottom, the velocity shifts of the Fe II emission increase. We find that FWHM(Hβ_{BC}) increases while the Fe II flux decreases, consistent with the correlations seen in §4.3. Inspecting the continuum slope, composite A shows a redder continuum than the rest (this can be seen most easily when comparing composites A with B). This suggests that sources with low v_{Fe}, which from our analysis are often accompanied by high L_{bol}/L_{Edd} and strong Fe II emission, tend to have redder UV-optical continua. This pattern is reminiscent of that seen by Constantin & Shields (2003), who found that the UV-optical continuum of NLS1s, which have high L_{bol}/L_{Edd} and strong Fe II, is redder than that of regular AGNs. This is unexpected from standard accretion disk models, since a higher L_{bol}/L_{Edd} generally produces a hotter disk and thus a bluer continuum (e.g., Hubeny et al. 2000, and references therein).

Note that it is difficult to see the shifts of the Fe II emission clearly in the composite spectra. For example, the peaks between $\sim$ 5150 and 5250 Å appear to remain unshifted. The reason is as follows. On the one hand, since both the shifts and widths of the Fe II emission have a large scatter in each subsample, stacking the spectra effectively smooths the Fe II emission. On the other hand, there are many narrow emission lines (e.g., line system N3 in Véron-Cetty et al. 2004) that are weak in a single spectrum and have nearly no shift. Stacking the spectra enhances these narrow features.

Another interesting phenomenon is that the wings of the Hβ profile become progressively more (red) asymmetric when v_{Fe} increases (Fig. 13). The inserted plot shows the difference spectra between composites B through E, using composite A as reference, to emphasize the profile changes. Note the systematic migration of the red excess as v_{Fe} increases. We do find some individual sources, similar to OQ 208 (Marziani et al. 1993), whose redshifted Hβ component seems to be associated with Fe II emission (§5.1). The asymmetry in Hβ has been studied by many authors. Boroson & Green (1992) found that there are Hβ red asymmetries at small R_{Fe}. Marziani et al. (1996) found that radio-loud AGNs show predominantly redshifted and red asymmetric Hβ profiles: the larger the shift, the broader the line. Recently, Netzer & Trakhtenbrot (2007) investigated the fractional luminosity of the red part of the Hβ line and found that it has a tendency to increase with decreasing Fe II/Hβ (see their Table 3). Considering that v_{Fe} inversely correlates with R_{Fe}, as shown in the right panel of Figure 9, the finding here is consistent with theirs. One possible interpretation, discussed in §5.2, is that the Hβ excess emerges from the same region that produces Fe II. A systematic study of this issue will be carried out in a future paper.

5. DISCUSSION

5.1. *Redshifted Hβ Component: OQ 208-like Quasars*

In our sample, we find a class of sources whose Hβ profile can be fitted well including an additional, substantially redshifted Gaussian component. Usually this additional com-
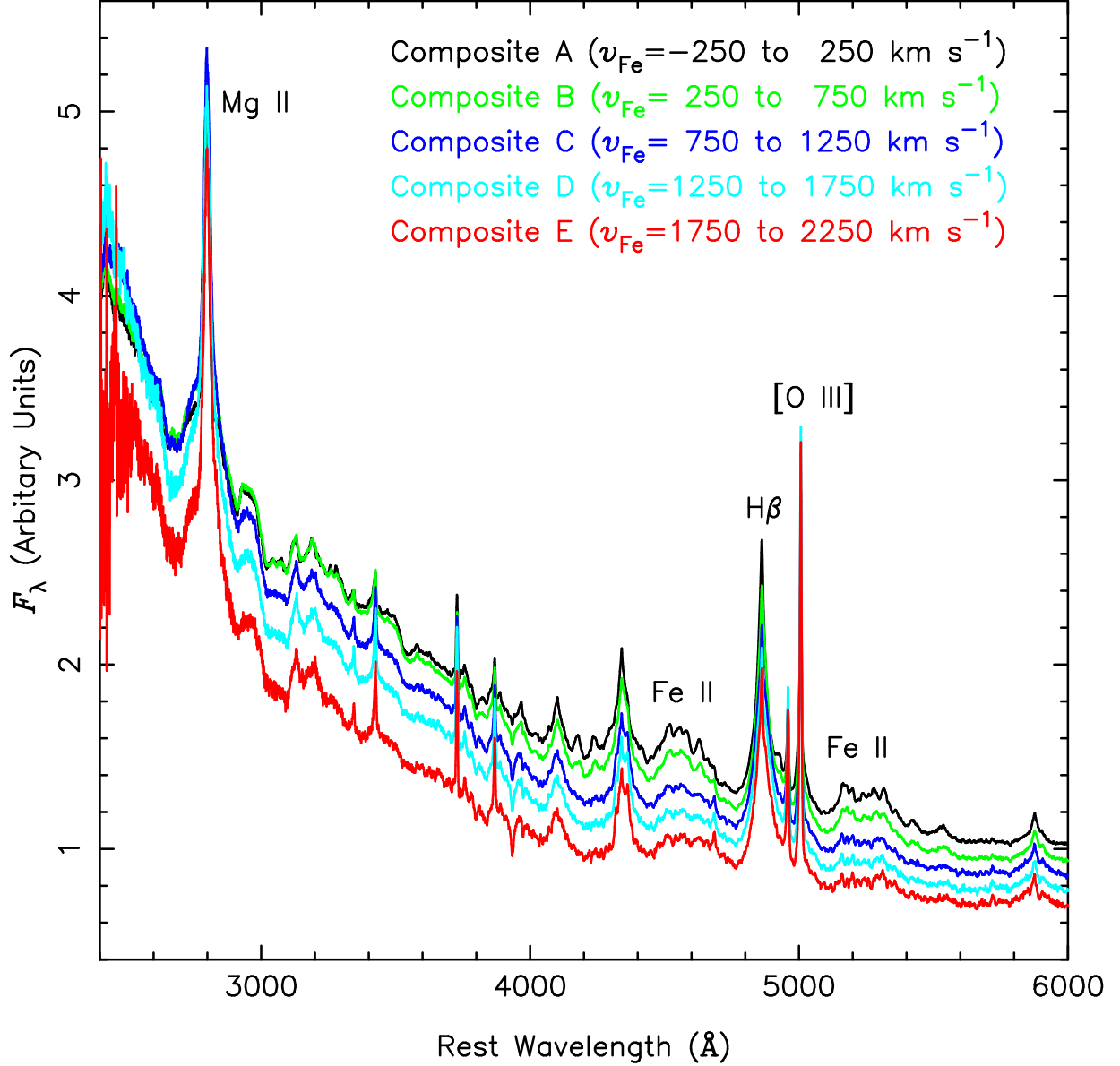
FIG. 12.— Composite spectra of quasars in bins of different v_{Fe}. See text for details on generating the composite spectra. We shifted the spectra vertically for clarity. Major emission lines are indicated; see Vanden Berk et al. (2001) for a complete identification of the emission lines.

ponent has a velocity width intermediate between that of the broad and narrow components. We call this the intermediate component. An interesting and possibly highly significant fact is that the width and velocity shift of this additional Hβ component is consistent with those of the Fe II emission. A prototype of this kind of sources is OQ 208 (Mrk 668), which was first studied in detail by Marziani et al. (1993). They pointed out that in OQ 208 the Fe II lines at 4924 and 5018 Å have the same peak displacement as the red peak of Hβ.

Figure 14 shows the spectrum of SDSS J094603.94+013923.6, an example of a OQ 208-like source. Panel (a) shows the continuum decomposition, following the same convention as used in the top panel of Figure 1. Panel (b) shows the emission-line spectrum after continuum subtraction. The red solid line is our Fe II model. The blue dashed line marks the position of the peak of Fe II λ4924 at zero velocity shift. The shift of the Fe II spectrum is obvious. Panel (c) illustrates the detailed fitting of the Hβ and [O III] emission lines. The profile of Hβ_{NC} is fixed to

that of [O III]. The two blue dashed lines mark the rest-frame wavelength of Hβ and [O III] λ5007; both Hβ_{NC} and [O III] share the same velocity. A prominent, intermediate-width redshifted component is clearly required to fit Hβ. Panel (d) shows the fit for [O II] λ3727, which also has the same redshift as [O III]. This means that this source is not an [O III] "blue outlier" (Boroson 2005). Table 3 lists the FWHMs and velocity shifts of Fe II, [O III], [O II], and each component of Hβ. The velocity shifts are all with respect to [O III]. The width and velocity shift of the redshifted Hβ component are consistent with those of Fe II emission. The emission-line spectrum of SDSS J094603.94+013923.6 can be divided into three systems: (1) Hβ, [O III], and [O II] emission lines with narrow (FWHM $\approx$ 500 km s^{-1}) widths and no velocity shift; (2) a normal "broad" Hβ component with FWHM $\approx$ 5700 km s^{-1}, approximately at rest with respect to the narrow lines; and (3) Fe II emission and Hβ of intermediate width (FWHM $\approx$ 1500 km s^{-1}) redshifted by $\sim$ 1500 − 1700 km s^{-1}.

TABLE 3
EMISSION-LINE PROPERTIES OF SDSS J094603.94+013923.6

	Fe	Redshifted	Broad	Narrow	[O III][a]	[O II]
		Hβ			
FWHM (km s^{-1})	1543(55)	1428(18)	5730(58)	$\cdots$ [b]	505(6)	568(18)
Velocity shift (km s^{-1})	1533(24)	1756(7)	373(25)	49(10)	$\cdots$ [c]	$-22(8)$

NOTE. — The number in parenthesis is the error.
[a] Refers to the line core component used to derive the redshift.
[b] The width of the Hβ$_{NC}$ is fixed to the width of [O III].
[c] The redshift of [O III] is used as the systemic redshift.
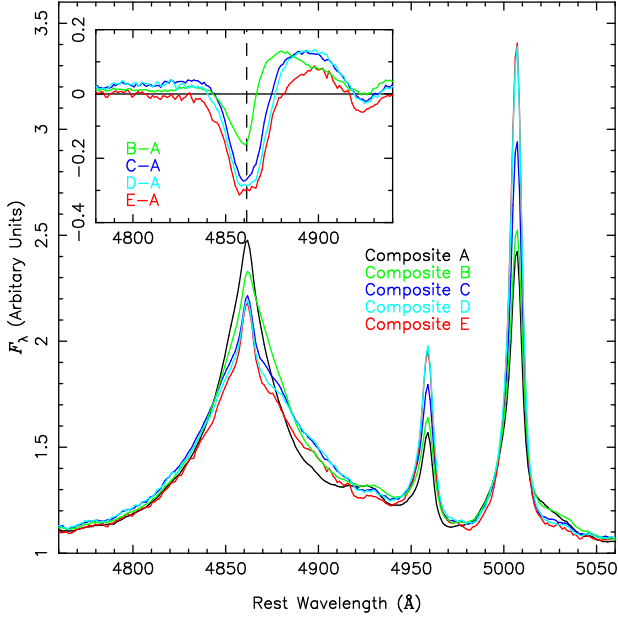
FIG. 13.— Hβ and [O III] region of the composite spectra. The inserted plot shows the difference spectra. The vertical dashed line is drawn at 4861 Å. Note the excess on the red wing of Hβ.

OQ 208-like sources can offer an unique view to understand the origin of Fe II emission and the structure of the BLR. A detailed study of this class of objects is beyond the scope of this paper. We will analyze a sample of such sources discovered in our work in a forthcoming publication. For the purposes of the present discussion, we simply note: Fe II emission is not associated with the conventional broad component of Hβ but instead originates from the same region emitting the intermediate component of Hβ. This is consistent with our findings in §4.1 that the width of Fe II is systematically narrower than that of Hβ$_{BC}$.

5.2. *Where is the Fe II Emission Region?*

This paper has demonstrated that Fe II emission most likely does not originate from the same location that produces the broad component of Hβ. The evidence comes from the systematic redshifts and narrower line widths of Fe II compared to Hβ$_{BC}$. As discussed below, the simplest interpretation is that Fe II emission originates from an inflow that is located at the outer parts of the BLR. The Hβ$_{BC}$ emission line itself shows no systematic velocity shift, and any velocity shift itself is also small. This suggests that Hβ$_{BC}$ emission region is well virialized and that the width of Hβ$_{BC}$ is dominated by gravity, making this line suitable for estimating BH masses.

Our finding that FWHM$_{Fe}$ $\approx$ 3/4 FWHM(Hβ$_{BC}$) suggests that the Fe II emission region is farther from the central BH than the Hβ$_{BC}$ emission region. If the Fe II emission region is

also virialized, so that $R \propto v^{-2}$, then it is about 2 times farther from the center than the Hβ$_{BC}$ region. On the other hand, the systematic redshift of Fe II indicates that the assumption of virialization may be incorrect.

The redward shift of Fe II and the inverse correlation between v_{Fe} and L_{bol}/L_{Edd} favor a scenario in which Fe II emission emerges from an inflow. To explain the systematic redshift, the inflow on the back side of the accretion disk must be obscured by the accretion disk and the torus, so that we can only observe the redshifted part on the nearer side. To explain the inverse correlation between v_{Fe} and L_{bol}/L_{Edd}, we speculate that the inflow is driven by gravity toward the center and decelerated by the radiation pressure. An increase in L_{bol}/L_{Edd} would enhance the radiation pressure and lead to a decrease of the inward velocity of the inflow.

Previous studies of the C IV line have shown that it tends to be systematically blueshifted (e.g., Gaskell 1982; Wilkes 1984; Marziani et al. 1996; Sulentic et al. 2000a; Richards et al. 2002b). This finding has led to suggestions that high-ionization lines and low-ionization lines originate from distinct regions (see also the result of reverberation mapping Peterson & Wandel 1999). High-ionization lines such as C IV may be emitted from some kind of outflowing disk wind (e.g., Leighly & Moore 2004; Leighly 2004; Baskin & Laor 2005; Shang et al. 2007, and references therein), whereas low-ionization lines such as Hβ are anchored to a more disk-like configuration. This paper adds an additional element to this picture. We suggest that in addition to a disk and a wind, the BLR has yet another component, one associated with inflowing material that produces the Fe II emission. Interestingly, Welsh et al. (2007) recently reanalyzed the spectral variability of the well-studied Seyfert 1 galaxy NGC 5548 and suggested, based on the differential lag between the red and blue wings of the Hβ profile, that the BLR in this object contains an inflowing component. Such an inflow is likely to develop from the inner edge of the dusty torus, which may connect with the accretion disk. If this picture is correct, the redshifted Fe II emission can be used as a probe of the transition region from the dusty torus to the BLR or accretion disk. More detailed theoretical modelling and observations of the Fe II emission region are clearly required to test this picture.

6. SUMMARY

Using a large sample of quasars selected from SDSS, we have studied the properties of their optical Fe II emission, especially their velocity profile and velocity shift, with the goal of understanding the origin of the nature of the Fe II-emitting region. This was accomplished using an improved iron template-fitting method, whose reliability has been tested using extensive simulations.

Our findings can be summarized as follows:

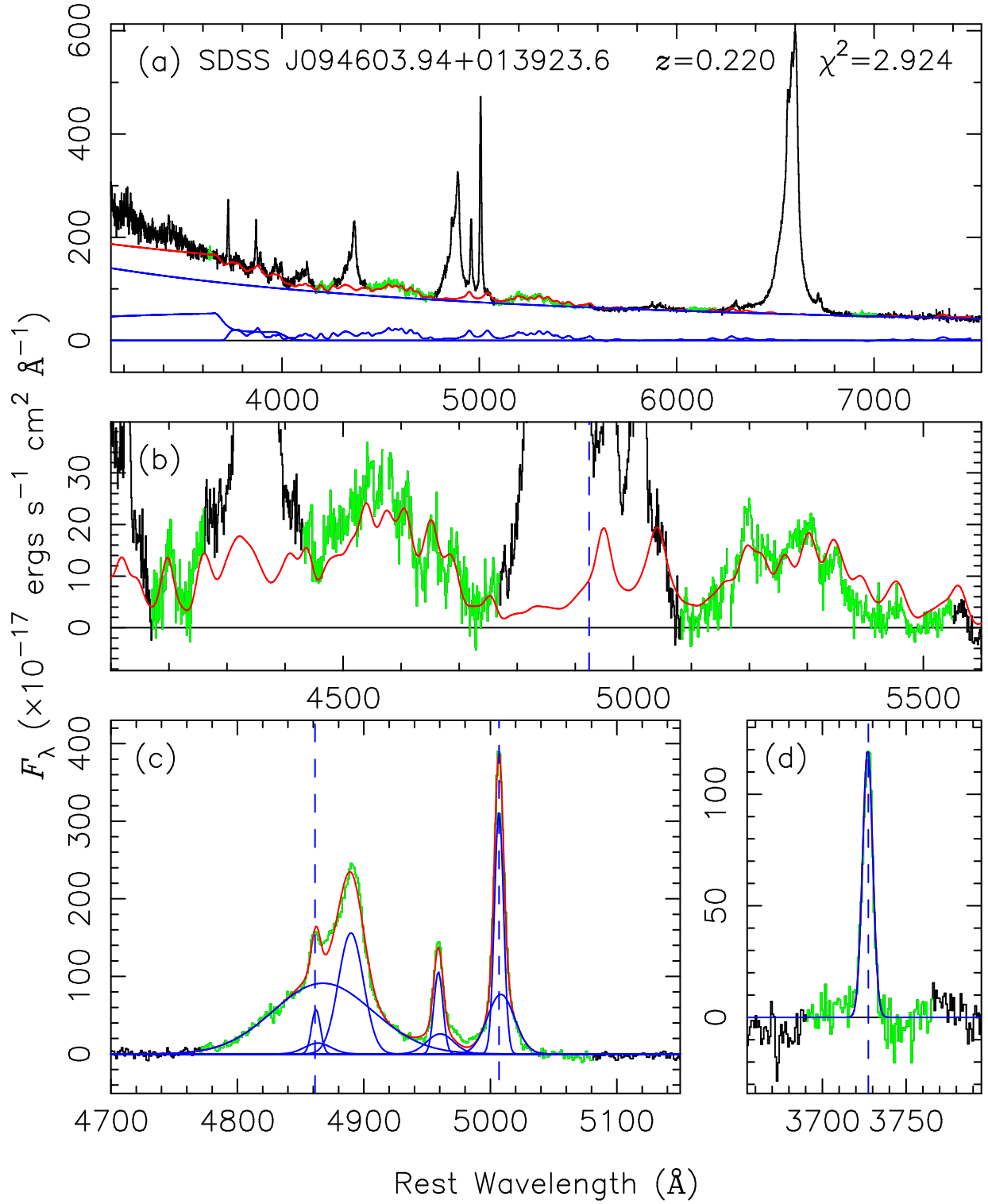1. The majority of quasars show redshifted Fe II emission

FIG. 14.— Spectrum of SDSS J094603.94+013923.6, an example of a OQ 208-like source. (*a*) Continuum decomposition. (*b*) Fe model and the observed spectrum after subtracting the power law and Balmer continuum. The spectra and the marks plotted in panel (*a*) and (*b*) are as the same as those in the top and bottom panels of Fig. 1. (*c*) Fitting of Hβ and [O III] emission lines. The multiple Gaussian components are in blue, and the sum of them is in red. The two blue dashed lines mark the rest-frame wavelength of Hβ and [O III] λ5007. (*d*) Fitting of [O II] emission line. The blue dashed line marks the rest-frame wavelength of [O II] λ3727. Note that the redshifts and widths of [O II], [O III], and Hβ$_{NC}$ are almost the same. Note also that we added an additional redshifted Gaussian line to fit Hβ. The width and velocity shift of this redshifted Hβ component are consistent with those of Fe II emission. See text and Table 3 for more details.

with respect to the systemic velocity of narrow-line region (as traced by [O III] λ5007) or of the conventional broad-line region (as traced by Hβ). The shift is typically ~ 400 km s^{-1} and can be as large as ~ 2000 km s^{-1}. By contrast, neither the broad Hβ nor Mg II lines show a systematic velocity shift.

2. The velocity width of Fe II is systematically narrower than that of the broad component of Hβ. On average, FWHM$_{Fe} \approx 3/4$ FWHM(Hβ_{BC}).

3. The velocity shift of Fe II increases with decreasing Eddington ratio, decreasing Fe strength, and increasing Hβ line width. No clear trends with radio or X-ray properties can be discerned.

4. Composite spectra reveal that objects with large Fe II velocity shifts have a tendency to exhibit asymmetric Hβ profiles with an excess red wing. This phenomenon is particularly notable in a subclass of objects that resembles the prototype OQ 208. The Hβ profile of OQ 208-like sources show a redshifted component of intermediate width that closely resembles the Fe II emission.

5. Our results strongly indicate that Fe II emission does not originate from the same region of the BLR that produces the "traditional" broad component of Hβ. Instead, we suggest that Fe II is associated with the intermediate-width Hβ component, both tracing an inflowing component of the BLR.

REFERENCES

Adelman-McCarthy, J., et al. 2007, ApJS, 172, 634
Baldwin, J. A., et al. 1996, ApJ, 461, 664
Baldwin, J. A., Ferland, G. J., Korista, K. T., Hamann, F., & LaCluyzé, A. 2004, ApJ, 615, 610
Baskin, A., & Laor, A. 2005, MNRAS, 356, 1029
Becker, R. H., White, R. L., & Helfand, D. J. 1995, ApJ, 450, 559
Boller, Th., Brandt, W. N., & Fink, H. 1996, A&A, 305, 53
Bonning, E. W., Shields, G. A., & Salviander, S. 2007, ApJ, 666, L13
Boroson, T. A. 2002, ApJ, 565, 78
——. 2005, ApJ, 130, 381
Boroson, T. A., & Green, R. F. 1992, ApJS, 80, 109
Bottorff, M., Korista, K. T., Shlosman, I., & Blandford, R. D. 1997, ApJ, 479, 200
Cardelli, J. A., Clayton, G. C., & Mathis, J. S. 1989, ApJ, 345, 245
Carswell, R. F., et al. 1991, ApJ, 381, L5
Collin-Souffrin, S., Hameury, J.-M., & Joly, M. 1988, A&A, 205, 19
Constantin, A., & Shields, J. C. 2003, PASP, 115, 592
Dietrich, M., Appenzeller, I., Vestergaard, M., & Wagner, S. J. 2002, ApJ, 564, 581
Dietrich, M., Hamann, F., Appenzeller, I., & Vestergaard, M. 2003, ApJ, 596, 817
Ferland, G. J., Peterson, B. M., Horne, K., Welsh, W. F., & Nahar, S. N. 1992, ApJ, 387, 95
Gaskell, C. M. 1982, ApJ, 263, 79
Gehrels, N. 1986, ApJ, 303, 336
Grandi, S. A. 1982, ApJ, 255, 25
Greene, J. E., & Ho, L. C. 2005a, ApJ, 627, 721
——. 2005b, ApJ, 630, 122
——. 2006, ApJ, 641, 117
Greene, J. E., Ho, L. C., & Ulvestad, J. S. 2006, ApJ, 636, 56
Hao, L., et al. 2005, AJ, 129, 1783
Hubeny, I., Agol, E., Blaes, O., & Krolik, J. H., 2000, ApJ, 533, 710
Ho, L. C. 2002, ApJ, 564, 120
Isobe, T., Feigelson, E. D., Akritas, M. G., & Babu, G. J. 1990, ApJ, 364, 104

Joly, M. 1987, A&A, 184, 33
——. 1991, A&A, 242, 49
Junkkarinen, V. 1989, in IAU. Symp. 134, Active Galactic Nuclei, ed. D. E. Osterbrock & J. S. Miller (Kluwer: Dordrecht), 122
Kaspi, S., Smith, P. S., Netzer, H., Maoz, D., Jannuzi, B. T., & Giveon, U. 2000, ApJ, 533, 631
Kim, M., Ho, L. C., & Im, M. 2006, ApJ, 642, 702
Kuehn, C. A., Baldwin, J. A., Peterson, B. M., & Korista, K. T. 2008, ApJ, 673, 69
Laor, A. 2000, ApJ, 543, L111
Laor, A., Fiore, F., Elvis, M., Wilkes, B. J., & McDowell, J. C. 1997a, ApJ, 477, 93
Laor, A., Jannuzi, B. T., Green, R. F., & Boroson, T. A. 1997b, ApJ, 489, 656
Leighly, K. M. 2004, ApJ, 611, 125
Leighly, K. M., & Moore, J. R. 2004, ApJ, 611, 107
Lupton, R. H. 1993, Statistics in Theory and Practice (Princeton: Princeton Univ. Press)
McGill, K. L., Woo, J.-H., Treu, T., & Malkan, M. A. 2008, ApJ, 673, 703
Maiolino, R., Juarez, Y., Mujica, R., Nagar, N. M., & Oliva, E. 2003, ApJ, 596, L155
Maoz, D., et al. 1993, ApJ, 404, 576
Marziani, P., Sulentic, J. W., Calvani, M., Perez, E., Moles, M., & Penston, M. V. 1993, ApJ, 410, 56
Marziani, P., Sulentic, J. W., Dultzin-Hacyan, D., Calvani, M., & Moles, M. 1996, ApJS, 104, 37
Marziani, P., Sulentic, J. W., Zamanov, R., Calvani, M., Dultzin-Hacyan, D., Bachev, R., & Zwitter, T. 2003b, ApJS, 145, 199
Marziani, P., Sulentic, J. W., Zwitter, T., Dultzin-Hacyan, D., & Calvani, M. 2001, ApJ, 558, 553
Marziani, P., Zamanov, R. K., Sulentic, J. W., & Calvani, M. 2003a, MNRAS, 345, 1133
Matsuoka, Y., Oyabu, S., Tsuzuki, Y., & Kawara, K. 2008, ApJ, 673, 62
McIntosh, D. H., Rix, H.-W., Rieke, M. J., & Foltz, C. B. 1999, ApJ, 517, L73

McLure, R. J., & Jarvis, M. J. 2002, MNRAS, 337, 109
——. 2004, MNRAS, 353, L45
Mukai, K. 1993, Legacy, 3, 21
Netzer, H., & Trakhtenbrot, B. 2007, ApJ, 654, 754
Netzer, H., & Wills, B. J. 1983, ApJ, 275, 445
O'Donnell, J. E. 1994, ApJ, 422, 158
Osterbrock, D. E., & Pogge, R. W. 1985, ApJ, 297, 166
Peterson, B. M., & Wandel, A. 1999, ApJ, 521, L95
Phillips, M. M. 1977, ApJ, 215, 746
Popović, L. Č., Smirnova, A., Ilić, D., Moiseev, A., Kovačević, J., & Afanasiev, V. 2007, in The Central Engine of Active Galactic Nuclei, ed. L. C. Ho & J.-M. Wang (San Francisco: ASP), 552
Press, W. H., Teukolsky, S. A., Vetterling, W. T., & Flannery, B. P. 1992, Numerical Recipes in FORTRAN (2nd ed.; Cambridge: Cambridge Univ. Press)
Richards, G. T., et al. 2002a, AJ, 123, 2945
——. 2002b, AJ, 124, 1
——. 2006, AJ, 131, 2766
Salviander, S., Shields, G. A., Gebhardt, K., & Bonning, E. W. 2007, ApJ, 662, 131
Schlegel, D. J., Finkbeiner, D. P., & Davis, M. 1998, ApJ, 500, 525
Schneider, D. P., et al. 2007, AJ, 134, 102
Shang, Z., Wills, B. J., Wills, D., & Brotherton, M. S. AJ, 2007, 134, 294
Sigut, T. A. A., & Pradhan, A. K. 1998, ApJ, 499, L139
Sigut, T. A. A., Pradhan, A. K., & Nahar, S. N. 2004, ApJ, 611, 81
Spergel, D. N., et al. 2007, ApJS, 170, 377
Storey, P. J., & Hummer, D. G. 1995, MNRAS, 272, 41
Sulentic, J. W., Bachev, R., Marziani, P., Negrete, C. A., & Dultzin, D. 2007, ApJ, 666, 757

Sulentic, J. W., Marziani, P., & Dultzin-Hacyan, D. 2000a, ARA&A, 38, 521
Sulentic, J. W., Zwitter, T., Marziani, P., & Dultzin-Hacyan, D. 2000b, ApJ, 536, L5
Tsuzuki, Y., Kawara, K., Yoshii, Y., Oyabu, S., Tanabé, T., & Matsuoka, Y., 2006, ApJ, 650, 57
Vanden Berk, D. E., et al. 2001, AJ, 122, 549
——. 2005, AJ, 129, 2047
van der Marel, R. P. & Franx, M. 1993, ApJ, 407, 525
Veilleux, S., & Osterbrock, D. E. 1987, ApJS, 63, 295
Verner, E., Bruhweiler, F., Verner, D., Johansson, S., Kallman, T., & Gull, T. 2004, ApJ, 611, 780
Véron-Cetty, M.-P., Joly, M., & Véron, P. 2004, A&A, 417, 515
Vestergaard, M., & Peterson, B. M. 2005, ApJ, 625, 688
Vestergaard, M., & Wilkes, B. J. 2001, ApJS, 134, 1
Voges, W., et al. 1999, A&A, 349, 389
——. 2000, IAU Circ., 7432, 1
Wang, J., Wei, J. Y., & He, X. T. 2005, A&A, 436, 417
Wang, T., Brinkmann, W., & Bergeron, J. 1996, A&A, 309, 81
Welsh, W. F., Martino, D. L., Kawaguchi, G., & Kollatschny, W. 2007, in The Central Engine of Active Galactic Nuclei, ed. L. C. Ho & J.-M. Wang (San Francisco: ASP), 29
Wheeler, J. C., Sneden, C., & Truran, J. W. 1989, ARA&A, 27, 279
Wilkes, B. J. 1984, MNRAS, 207, 73
Wills, B. J., Netzer, H., & Wills, D. 1985, ApJ, 288, 94
Woo, J.-H., Treu, T., Malkan, M. A., & Blandford, R. D. 2006, ApJ, 645, 900
York, D. G., et al. 2000, AJ, 120, 1579